JGR Atmospheres

RESEARCH ARTICLE
10.1029/2021JD035005

Key Points:

- The gridded temperature data identify a new extreme cold wave (ECW) cluster over the Qinghai–Tibetan Plateau
- The Northern Annular Mode–like daily planetary wave patterns contribute more to the anomalous circulation producing ECWs than others
- The increasing trend of ECW occurrence over the Chinese mainland is attributable to the Northern Annular Mode–like daily planetary wave

Supporting Information:

Supporting Information may be found in the online version of this article.

Correspondence to:

Z. Xie,
xiezuowei@mail.iap.ac.cn

Citation:

Zhang, L., Xie, Z., Deng, Y., & Huang, W. (2021). Structure and large-scale organization of extreme cold wave events over the Chinese mainland during the boreal cold season. *Journal of Geophysical Research: Atmospheres*, *126*, e2021JD035005. https://doi.org/10.1029/2021JD035005

Received 2 APR 2021
Accepted 27 OCT 2021

Author Contributions:

Conceptualization: Z. Xie
Formal analysis: L. Zhang, Z. Xie
Investigation: L. Zhang
Methodology: L. Zhang
Supervision: Y. Deng
Writing – original draft: L. Zhang
Writing – review & editing: Z. Xie

Structure and Large-Scale Organization of Extreme Cold Wave Events Over the Chinese Mainland During the Boreal Cold Season

L. Zhang[1], Z. Xie[2], Y. Deng[3], and W. Huang[4]

[1]College of Biology and Environment, Nanjing Forestry University, Nanjing, China, [2]International Center for Climate and Environment Sciences, Institute of Atmospheric Physics, Chinese Academy of Sciences, Beijing, China, [3]School of Earth and Atmospheric Sciences, Georgia Institute of Technology, Atlanta, GA, USA, [4]Ministry of Education Key Laboratory for Earth System Modeling, Department of Earth System Science, Tsinghua University, Beijing, China

Abstract Recent changes in the Earth's climate have led to renewed interest in extreme cold wave (ECW) events. This study identifies the ECW patterns over the Chinese mainland, their corresponding large-scale meteorological patterns (LMPs) and their favorable planetary wave patterns over 1961–2015. A self-organizing map classifies ECWs into northeast, nationwide, northwest–south and Qinghai–Tibetan Plateau clusters. The cold anomalies are primarily contributed by the anomalous wind advecting climatological mean temperature for the leading three clusters, but diabaitic heating for the Qinghai–Tibetan Plateau cluster. The associated LMPs are primarily characterized by a dipole with a positive height anomaly over Siberia and a negative height anomaly extending from Japan to the Iranian Plateau, which displaces southwestward among the four ECW clusters. The LMPs induce anomalous northerly flows extending from the upper troposphere to the near-surface, which deepen the negative height anomaly southwestward from the East Asian trough and accumulate cold air masses over the key regions within the dipole that are phase-locked with the LMPs (i.e., baroclinic growth). Such baroclinic growth of the LMP is larger during periods of a planetary wave (wavenumbers 1–5) resembling the Northern Annular Mode (NAM). Meanwhile, the negative (positive) phase of the NAM provides more direct contribution to the LMP of the northeast and nationwide (Qinghai-Tibetan Plateau) ECW clusters and thus are likely to favor the occurrence of ECWs. The negative phase of NAM-like planetary waves exhibit a positive trend after the transition year of 1987, and could potentially increase the occurrence frequency of nationwide ECWs.

1. Introduction

Extreme cold wave (ECW) events can impose serious damage to both human society and natural ecosystems (Ding et al., 2016; Hou et al., 2018). Recent anomalous warming of the Arctic region with global climate change has reduced winter surface air temperatures (SATs) over mid latitudes and stimulated a renewed interest in ECW events (Liang et al., 2014; Ma & Zhu, 2019; Qian et al., 2018; Tajie et al., 2020; Wang & Chen, 2014; Wang et al., 2017; Wu et al., 2017; Yu & Zhang, 2015), especially their distinct clusters and the associated circulations (Deng et al., 2020; Wu & Ren, 2021; Xie et al., 2017a). Two sequential ECW events engulfed the Chinese mainland during the periods December 29, 2020–January 1, 2021 and January 6–8, 2021, delivering extreme, record-setting winter weather to 58 cities, and were tied to the warm Arctic and the cold tropical Pacific (Bueh et al., 2021).

Extreme cold wave (ECW) events over the Chinese mainland show diverse patterns (Liu et al., 2020, 2021; Wang et al., 2013; Zhang & Qian, 2011). Using observational data from ground-based stations, Peng and Bueh (2011) identified five long-lived ECW groups by applying a *K*-mean clustering analysis to the SATs on the ECW peak days over the Chinese mainland. According to their geographical distributions, these five ECW clusters are named as the nationwide cluster, the eastern cluster, the northeast–north cluster, central–eastern cluster and northwest–south cluster. A parallel analysis applying empirical orthogonal function decomposition to the long-lived ECWs further confirmed these ECW groups (Wu & Ren, 2021). Similar ECW patterns and more clusters with regional features have been identified based on the geographical distribution of long-lived ECW events (Qian, 2012; Wang & Chen, 2014). These studies of ECW clustering have been based on observational data from ground-based stations, which are primarily distributed over eastern

Cina. Since the clustering analysis is mainly based on the Euclidian distance of the SAT at each station, the ECW clusters tend to be seen over eastern China. Although ECW events have been explored using gridded SAT data (Liu et al., 2020; Song & Wu, 2017), they are defined based on the mean SAT over fixed regions and the typical ECW patterns remain unclear. Compared to prior studies using irregular ground-based data, the advantage of this study is its use of gridded data to capture the ECW patterns.

The large-scale meteorological pattern (LMP) refers to the *daily* scale circulation anomaly that is directly associated with extreme ECW events (Grotjahn et al., 2016). The spatial scale of LMP is between that of synoptic systems and planetary-scale climate modes. It has been well recognized that ECW events over the Chinese mainland are closely related to blocking over Eurasia, particularly over the Ural Mountains (Cheung et al., 2012, Cheung, Zhou, Shao, et al., 2013; Ji et al., 2008; Luo et al., 2016; Ma & Zhu, 2019; Tao, 1959; Ye et al., 1962). However, not all ECW events are related to blocking, and the LMP includes a portion that superficially resembles blocking (Grotjahn et al., 2016; Xie & Bueh, 2017). Some studies have tied ECW events with the East Asian trough (Leung & Zhou, 2015; Wang et al., 2009) or a wave train pattern over the Eurasian continent (Park et al., 2011; Song & Wu, 2017; Takaya & Nakamura, 2005). Given an unprecedented persistent ECW event in January 2008, researchers noted that such persistent ECW events are attributable to a pair of large-scale tilted ridges and troughs over the Eurasian continent rather than a single block or trough (Bueh & Xie, 2015; Bueh et al., 2011; Wu & Ren, 2021). The configuration of the large-scale tilted ridges and troughs also varies among the ECW groups (Bueh et al., 2015; Song & Wu, 2017). Although previous studies have identified LMPs for ECW events over the Chinese mainland, they have primarily been top-down analyses from a preferred circulation or bottom-up analyses from rare ECW events. We aim to isolate the LMPs for the ECW clusters over the Chinese mainland in this study.

The Observing System Research and Predictability Experiment: a World Weather Research Program (THORPEX) project noted that planetary waves with zonal wavenumbers within 1–5 can improve the predictability of high-impact weather as they bridge remote forcing and regional synoptic-scale disturbances (Shapiro & Thorpe, 2004). Much of the current literature on the relationship between the ECW events over the Chinese mainland and planetary waves pays particular attention to the Arctic Oscillation/Northern Annular Mode (AO/NAM; Chen & Kang, 2006; Park et al., 2010, 2011; Yuan & Li, 2019). The NAM is the mid- and upper tropospheric manifestation of the near-surface AO, which is the leading climate mode in winter in the Northern Hemisphere (Thompson & Wallace, 1998). ECW events over northern China are likely to occur during negative phase of the NAM (Chen & Kang, 2006; Gong et al., 2001; Jeong & Ho, 2005; Liu et al., 2012). The negative NAM phase induces ECW events via blocking or a dipole circulation and an amplified Siberian high (He, 2015; Park et al., 2010, 2011; Yuan & Li, 2019). By contrast, Liang et al. (2019) showed that the positive NAM phase increases the occurrence of ECW events over southern China by deepening the southern branch trough. The monthly and daily AO/NAM indices used in these studies represent the index of total anomalies projecting onto the AO/NAM pattern and thus are not isolated from the LMP. Based on the truncated daily 500-hPa geopotential height (Z500) field with wavenumbers 1–5, Xie et al. (2017b) identified six daily planetary wave patterns during the boreal cold season. Xie, Black, and Deng (2019) demonstrated that these daily planetary waves provide direct and indirect contributions, which promotes both barotropic and baroclinic growth of synoptic waves to the LMP enacting ECWs over the United States. Therefore, there is a need to investigate what daily planetary waves are favorable for ECW clusters over the Chinese mainland and their contributions to LMPs.

We note that earlier studies have identified LMPs mainly on the basis of ECW events defined using ground-based stations data. However, the spatial heterogeneity of ground-based stations data leads to a bias toward ECW patterns over Eastern China. We aim to systematically identify the ECW clusters by applying a self-organizing map (SOM; Kohonen, 2001) approach to gridded SAT data over the Chinese mainland during ECWs. We then use this classification to define their associated LMPs in terms of the composite Z500 anomaly and their potential linkages to daily planetary waves, which are wavenumbers 1–5 of Z500. The contributions of daily planetary waves to the LMP are assessed using a pattern amplitude projection (Deng et al., 2012) and a baroclinic energy conversion during periods associated with different planetary waves. Based on the relationship between planetary waves and the LMP, the long-term variabilities of planetary waves are used to interpret the trend of ECW occurrence number. We describe our data and methods in Section 2. Section 3 presents the ECW patterns, associated heat budget analysis and circulation features. Section 4 discusses the relationships between LMPs and daily planetary waves. The final section gives our summary and discussion.

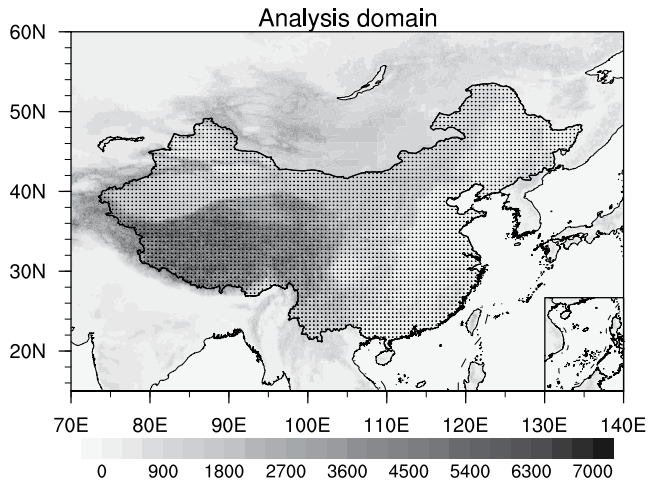

Figure 1. Analysis domain of the Chinese mainland (black line) and distribution of the 3816 grid points (dots) used in our analysis. Shading indicates topography (unit: m).

2. Data and Methods

2.1. Data

We use the daily mean SAT on a (0.5° × 0.5°) latitude–longitude grid provided by the Asian Precipitation–High Resolved Observational Data Integration Toward Evaluation of Water Resources (APHRODITE) project (Yasutomi et al., 2011) to identify ECW events. This gridded SAT dataset is interpolated from station observations collected from the Global Telecommunication System datasets, pre-compiled datasets from other organizations or groups, and individual collections. The raw SATs are applied to an automated quality control system and then interpolated onto grids using a distance-weighting function based on Spheremap. This APHRODITE SAT product covers the region of (15°S–55°N, 60°–155°E) for the period 1961–2015.

We also use several different meteorological fields from the fifth generation European Center for Medium-range Weather Forecasts (ECMWF) reanalysis dataset (ERA5; Hersbach et al., 2020). The air temperature at 2 m above the surface and the horizontal wind at 10 m above the surface on a (0.5° × 0.5°) longitude–latitude grid are used to compare these datasets with APHRODITE. The other variables used in this study are sea level pressure (SLP), the geopotential height, horizontal winds, and potential vorticity at different pressure levels on a (2.5° × 2.5°) longitude–latitude grid. The pressure levels adopted here are equally spaced every 50 hPa between 1,000 and 100 hPa. The potential temperature and horizontal winds at the dynamic tropopause (2 PVU, 1 PVU = 10^{-6} m^2 s^{-1} K kg^{-1}) from ERA40 during 1961–1978 and ERA5 during 1979–2015 are used to explore dynamic aspects of the LMP. The boreal cold season refers to the period from November 1 to March 31 of the following year (151 days).

2.2. Definition of an ECW Event

We consider 3816 APHRODITE grid points within the Chinese mainland (Figure 1). An ECW event is identified using the APHRODITE SAT based on the following three criteria. Unlike prior studies focusing on relatively long-duration ECW events, we identify more ECW events to isolate robust ECW patterns.

1. *An extreme cold grid point*. An extreme cold grid point is recorded when the SAT is lower than the threshold value of the fifth percentile. For each calendar day, the percentile-based threshold value is calculated from a moving window of 5 consecutive days centered on that calendar day for the 30 base years using the quantile definition proposed by Hyndman and Fan (1996). The 30-year data are constructed with a simple bootstrap method using the 29-year base period data for 1974–2002, with 1 year repeated from this base period (Zhang et al., 2005). The average of the threshold values for the fifth percentile over the Chinese mainland corresponds to an overall standard deviation of −1.63.
2. *An extreme cold day*. An extreme cold day is recorded if the total number of extreme cold grid points is >10% of the total number of grid points (i.e., 382 grid points; Bueh et al., 2011; Xie et al., 2017a).
3. *An ECW event*. An ECW event is defined when there are at least three consecutive extreme cold days. Since there is a spatial coverage criterion of extreme grid points, there could be one day between two adjacent ECW events when the total number of extreme grid points is below the criterion. Therefore, the two adjacent ECW periods that are separated by one day are combined to form a single ECW event (Peng & Bueh, 2011; Takaya & Nakamura, 2005).

Accordingly, 192 ECW events are identified with a total of 1286 days, including 50 extensive and persistent ECW events (52 events in total) defined by Peng and Bueh (2011). The occurrence frequency of ECW events over the 54 boreal cold seasons is mainly distributed over Northwest and East China (Figure 2).

2.3. Clustering ECWs With the SOM

The SOM is an unsupervised learning-based artificial neural network (Kohonen, 2001). It maps high-dimensional data to a low-dimensional representative space with a neuronal structure, in which the neighboring

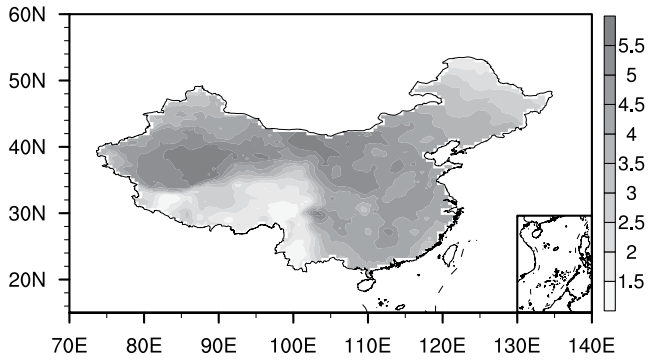

Figure 2. Distribution of the occurrence frequency of extreme cold wave (ECW) events over the 54 boreal cold seasons (unit: %).

SOM patterns have a geometric similarity. A batch SOM is applied to normalized SAT anomalies on 1286 ECW days by implementing MATLAB software with SOM Toolbox version 2.0 (www.cis.hut.fi/projects/somtoolbox/about). The SAT anomalies of 3816 grid points within the Chinese mainland on each ECW day are normalized by the climatological mean and standard deviation and then converted to a row vector. A specified number of random nodes/neurons are initialized with a weight vector and a position in the 2D map space. In each training step, 1286 vectors are partitioned according to the Voronoi region of the map weight vectors.

The next step is to update the nodes by averaging the data samples in the neighborhood of the best-matching unit. The best-matching unit is the node/neuron with the closest weight vector (in Euclidian space) to the partitioned input vectors. The output is an SOM with a prescribed number of nodes that represent the spatial patterns of the input SAT anomalies. An SOM with a larger number of nodes, therefore, provides a better description of the input SAT patterns. The optimum number of SOM patterns should be large enough to accurately capture the SAT patterns but small enough to be sufficiently different from each other. To determine the optimum number of SOM nodes, we repeat the SOM with grid numbers from (1 × 2) to (1 × 20) and compute the average pattern correlations between each row vector of normalized SAT anomalies and their corresponding centroids (Lee & Feldstein, 2013). The mean distance between each cluster pair is calculated in a slight adaptation of Wards' distance (Lee et al., 2017; Ward, 1963).

The SOM clustering indices are used to composite the meteorological anomaly fields to isolate the spatial structure and synoptic patterns for each ECW cluster. The Student's *t*-test is adopted to assess the statistical significance of the composite anomalies (Wilks, 2006).

2.4. Heat Budget Analysis

To explore relative contributions by physical processes to the near-surface cold air temperature anomalies, we apply an isobaric thermodynamic equation to two days before and to the ECW days, which are conducive to the cold SAT anomaly on the ECW days. The heat budget equation given by He and Black (2016) is as follows:

$$\frac{\partial T'}{\partial t} = -V' \cdot \nabla \overline{T} - \overline{V} \cdot \nabla T' - \left(V' \cdot \nabla T' - \overline{V' \cdot \nabla T'}\right) + S_p \omega' + \frac{Q'}{C_p} \tag{1}$$

where T is the air temperature, V is the horizontal velocity, S_p is the static stability parameter, ω is the vertical velocity, Q is the diabatic heating, and C_p is the specific heat of air at constant pressure. The primes represent anomalies relative to the climatology-mean values (the overbar). The local temperature anomaly tendency is contributed by an anomalous horizontal wind advecting climatological-mean air temperature ($-V' \cdot \nabla \overline{T}$), the climatological wind advecting air temperature anomalies ($-\overline{V} \cdot \nabla T'$), nonlinear process $-\left(V' \cdot \nabla T' - \overline{V' \cdot \nabla T'}\right)$, anomalous adiabatic heating ($S_p \omega'$), and anomalous diabatic heating (Q'/C_p).

2.5. Rossby Wave Activity Flux

We adopt the Rossby wave activity flux defined by Takaya & Nakamura (2001) to depict the horizontal energy propagation of atmospheric circulation anomalies relative to the climatological mean associated with the ECW events. The Rossby wave flux in the spherical coordinate is expressed as:

$$W = \frac{p\cos\phi}{2|\boldsymbol{U}|}\begin{Bmatrix} \frac{U}{a^2\cos^2\phi}\left[\left(\frac{\partial\psi'}{\partial\lambda}\right)^2 - \psi'\frac{\partial^2\psi'}{\partial\lambda^2}\right] + \frac{V}{a^2\cos\phi}\left[\frac{\partial\psi'}{\partial\lambda}\frac{\partial\psi'}{\partial\phi} - \psi'\frac{\partial^2\psi'}{\partial\lambda\partial\phi}\right] \\ \frac{U}{a^2\cos\phi}\left[\frac{\partial\psi'}{\partial\lambda}\frac{\partial\psi'}{\partial\phi} - \psi'\frac{\partial^2\psi'}{\partial\lambda\partial\phi}\right] + \frac{V}{a^2}\left[\left(\frac{\partial\psi}{\partial\phi}\right)^2 - \psi'\frac{\partial^2\psi'}{\partial\phi^2}\right] \end{Bmatrix}, \tag{2}$$

Table 1
The Zonal and Meridional Wavenumbers for the Triangular Truncation of Spherical Harmonic Analysis

Meridional wavenumber					
Zonal wavenumber	(0, 0)				
		(1, 0)			
	(0, 1)		(2, 0)		
		(1, 1)		(3, 0)	
	(0, 2)		(2, 1)		(4, 0)
		(1, 2)		(3, 1)	(5, 0)

where $\mathrm{U} = (\mathrm{U}, \mathrm{V})$ is the climatological mean flow velocity, which is taken to be the cold season average of the climatological mean (the long-term daily climatology of the period 1961–2015); Ψ' is the quasi geostrophic stream function perturbations relative to the climatological mean; a, φ and λ are the Earth's radius and the latitude and longitude, respectively; and p is the air pressure normalized by 1,000 hPa.

2.6. Planetary Wave Patterns

We adopt six planetary wave patterns from Xie et al. (2017b), which were derived by applying agglomerative hierarchical clustering to the truncated daily Z500 with wavenumbers 1–5. To focus on the Northern Hemisphere, the daily Z500 is assumed to have a symmetrical distribution about the equator and spherical harmonic decomposition is performed. A triangular truncation with wavenumber 5 without the wavenumber (0, 0) is applied to derive the daily planetary wave (Table 1). The wavenumber (0, 0) refers to wavenumber 0 in both the zonal and meridional components and represents the areal mean of the Northern Hemisphere. This wavenumber is removed to compare planetary waves on different calendar days. Six daily planetary wave patterns over 1950–2005 are identified based on the largest sequential jump in cluster distance. Daily planetary waves are categorized into six clusters according to the nearest Euclidian distance between each daily planetary wave (1961–2015) and the pre-defined cluster-mean composite planetary wave patterns.

3. Circulation Features of ECW Events

3.1. ECW Clusters

We repeated the SOM with grid numbers varying from (1 × 2) to (1 × 20) to identify the optimum separation of the ECW patterns. Figure 3 shows the mean correlation between the SAT anomalies on each ECW day and the corresponding cluster centroid as well as the mean distance between each pair of cluster centroids. The correlation increases greatly from (1 × 2) to (1 × 4) and then increases more smoothly, whereas the distance clearly decreases from (1 × 2) to (1 × 3) and then decreases only slightly. The combination of these two objective measures suggests that the (1 × 4) SOM grid has the optimum number of ECW clusters. Because our aim is to isolate the patterns of ECW events, we choose the (1 × 4) SOM grid rather than the (2 × 2) grid. To further test the robustness of the ECW clusters, we carried out sensitivity experiments by perturbing the extreme threshold value in the ECW definition criterion from the tenth to twentieth percentiles in five percentile steps without any qualitative change in the results. Taking the twentieth percentile for example, the spatial correlations between the obtained ECW patterns and counterparts of the fifth percentile are 0.96, 0.92, 0.87, and 0.75, respectively.

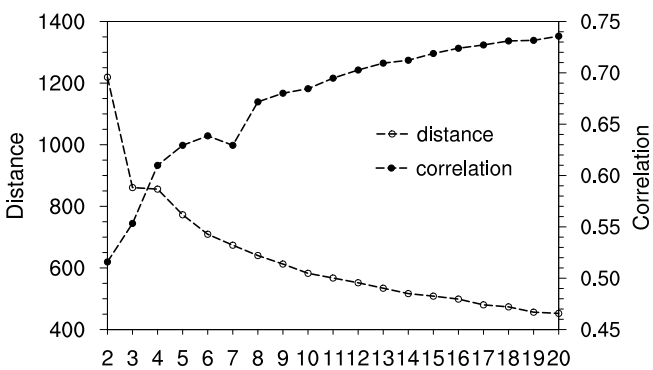

Figure 3. Mean correlation between the surface air temperature (SAT) anomalies on each extreme cold wave (ECW) day and the corresponding cluster centroid (closed circles) and the mean distance between each pair of cluster centroids (open circles).

Figure 4 shows the composite SAT anomaly patterns for four ECW clusters obtained from the APHRODITE and ERA reanalysis datasets. The near-surface winds are only shown for the ERA reanalysis data because they are unavailable in the APHRODITE data set. The four ECW patterns are characterized by cold SAT anomalies dominating over the Chinese mainland, with a southwestward displacement from Northeast China to West China and SAT magnitude decreasing among clusters 1–4, which is highly consistent between the APHRODITE and ERA datasets. The most common ECW pattern, which appears for 389 days, features a predominant cold SAT anomaly over the whole of China, except for the Tibetan Plateau (Figures 4a and 4e). The cold core, with a temperature of less than −8°C, occurs over Northeast China. This pattern is associated with northerly wind anomalies extending from Lake

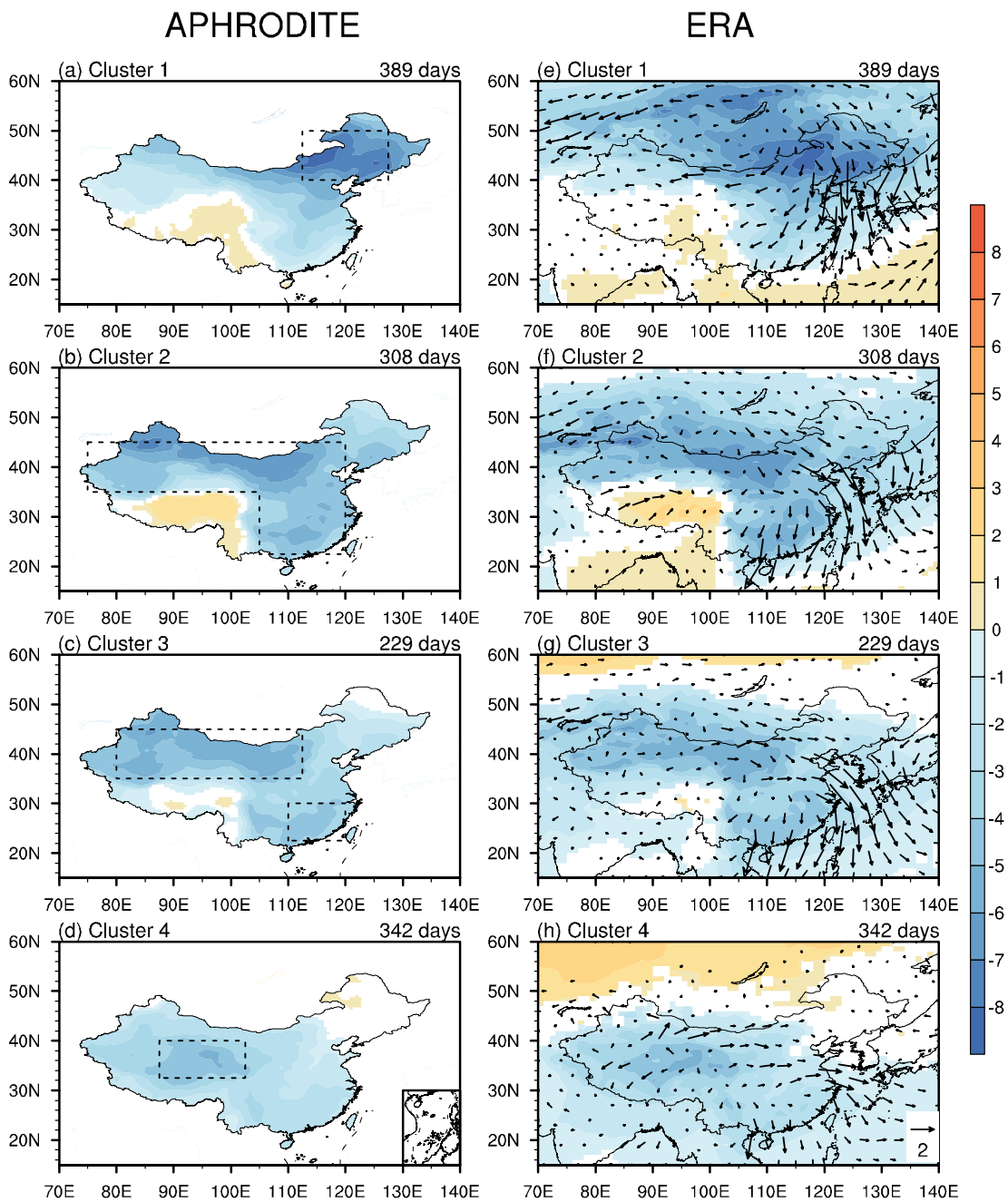

Figure 4. Composite APHRODITE SAT anomalies (shading; unit: °C) for (a) cluster 1, (b) cluster 2, (c) cluster 3 and (d) cluster 4. Composite ERA 2-m SAT anomalies (shading; unit: °C) for (e) cluster 1, (f) cluster 2, (g) cluster 3 and (h) cluster 4 overlain with the 10-m surface horizontal wind anomalies (arrows; units: m s^{-1}). The black boxes are the cold anomaly centers for each cluster. Only composite anomalies that are statistically significant at the 95% confidence level are shown.

Baikal to southern China, which transport cold air into Northeast and South China. In contrast with the first pattern, the cold SAT anomalies of the second cluster (308 days) shift southwestward, with two cold centers over Northwest and South China (Figures 4b and 4f). This feature is linked to anomalous northwesterly flows from Mongolia to Northwest China and northerly flows to South China. The warm anomaly over the Tibetan Plateau is more evident and is advected by a southwesterly wind anomaly. The third ECW pattern (229 days) resembles the second ECW pattern but with smaller amplitudes and a displacement slightly southwestward (Figures 4c and 4g). The cold anomaly center over the Junggar Basin extends southward to the Tarim Basin and is conveyed by northerly wind anomalies, and the warm

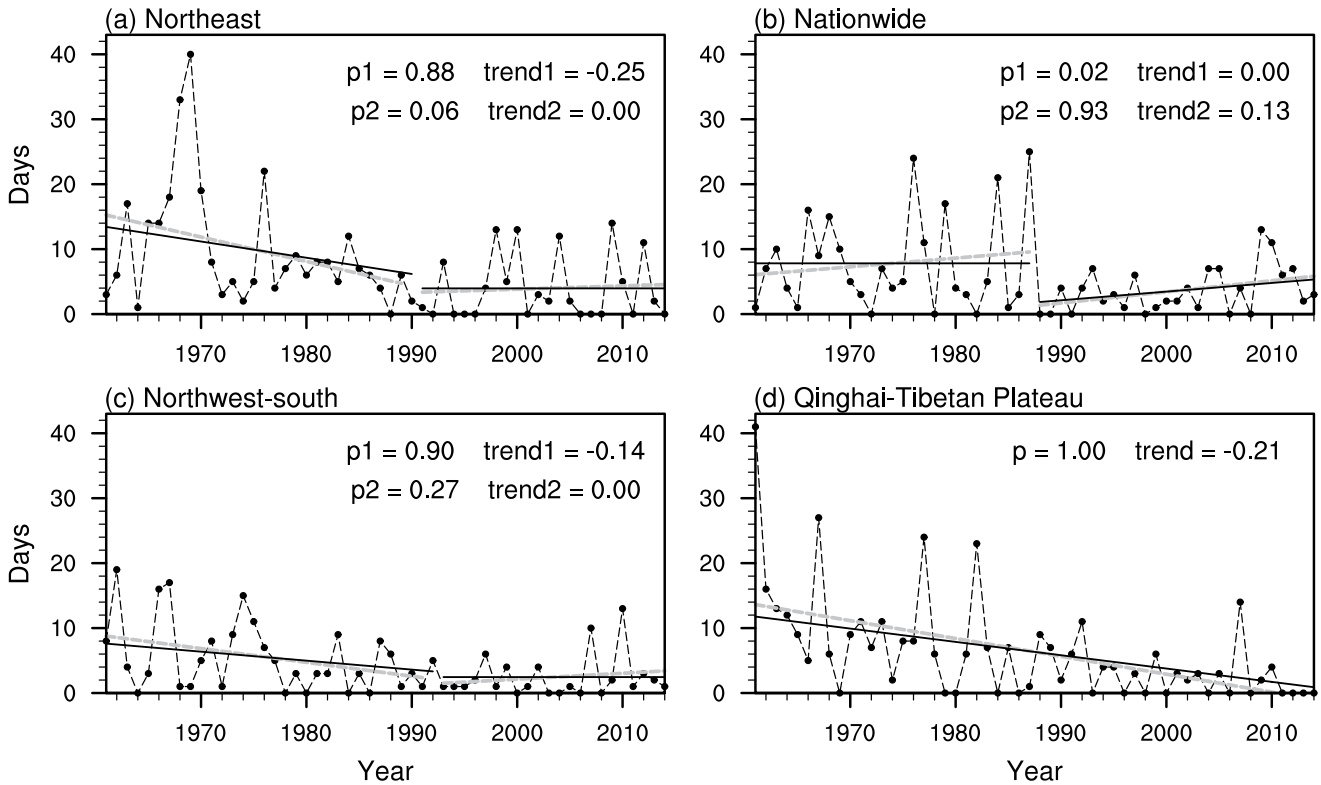

Figure 5. Time series of the occurrence numbers (dashed line with closed circles) for (a) the northeast extreme cold wave (ECW) cluster, (b) the nationwide ECW cluster, (c) the northwest–south ECW cluster and (d) the Qinghai–Tibetan Plateau ECW cluster. The gray dashed lines represent the linear regressions and the black solid lines are the Theil–Sen estimates of the linear trend. "*p*" is the significance level and "trend" is the trend of the Theil–Sen estimate.

anomaly over the Tibetan Plateau is weaker than that in the second cluster. The fourth pattern (342 days) contrasts with the first pattern, with the negative SAT anomaly concentrated over the Qinghai–Tibetan Plateau (Figures 4d and 4h). Unlike clusters 1–3, northerly wind anomalies are not seen over the cold anomaly center. This suggests that the cold anomaly of the fourth pattern may result from diabatic heating rather than cold SAT advection.

A parallel *K*-mean clustering (Wilks, 2006) with $K = 4$ shows that the ECW patterns are entirely consistent with our SOM clustering results, in which the pattern correlation coefficients are 0.95, 0.99, 0.80, and 0.98, respectively. The relatively low correlation in cluster 3 is because the cold anomaly center over South China is absent in the *K*-mean result, in which the ECW pattern is more isolated. Given the respective distributions of the cold SAT anomalies, the first three patterns are in good agreement with the patterns derived in previous studies using observational data from monitoring stations (Peng Bueh, 2011; Qian, 2012; Wang et al., 2013), which are referred to as northeast, nationwide, and northwest–south clusters. Our new fourth pattern suggests that, as expected, the spatial distribution of the ground-based meteorological stations has a strong impact on the classification of ECW events. Following the ECW definition of these studies, the ECW clusters 1–4 are denoted as northeast, nationwide, northwest–south, and Qinghai–Tibetan Plateau ECWs, according to the respective distributions of the cold SAT anomaly centers.

Figure 5 shows the time series of the annual occurrence frequency of the four clusters and derived trend lines. Noting the effect of climate change in previous studies (Zhang & Qian, 2011; Zhou & Ren, 2010), we use the Mann–Kendall test (Fu & Wang, 1992) to detect abrupt change in the annual ECW occurrence number. There are significant transitions in clusters 1–3 for the transition years of 1990, 1987, and 1992, respectively, while not in cluster 4 (Figure S1 in the supplement). We therefore separate the study period into two subperiods based on the transition year and calculate the trend during each subperiod for clusters 1–3. There are decreasing trends prior to the transition years for the northeast and north-

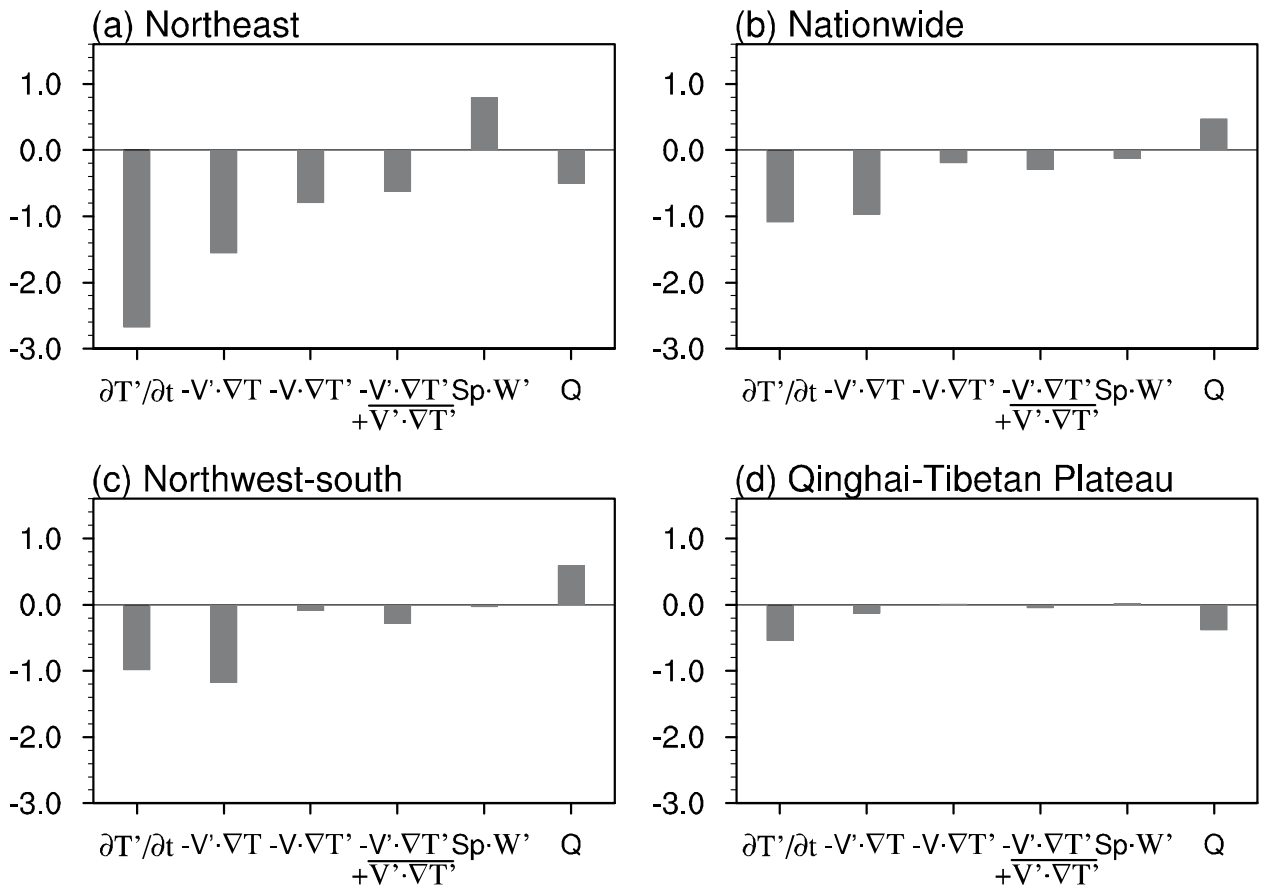

Figure 6. The composite air temperature tendency (units: °C d^{-1}) and the air temperature tendency due to $-V' \cdot \nabla \bar{T}$, $-\bar{V} \cdot \nabla T'$, $-\left(V' \cdot \nabla T' - \overline{V' \cdot \nabla T'}\right)$, $S_p \omega'$, and (Q'/C_p) forcings based on the heat budget analysis at 950 hPa averaged during days 2–0 and within each cold anomaly center in Figure 4 for (a) the northeast extreme cold wave (ECW) cluster, (b) the nationwide ECW cluster, (c) the northwest-south ECW cluster and (d) the Qinghai-Tibetan Plateau ECW cluster.

west–south ECWs, with the latter cluster significant at the 90% confidence level (Figures 5a and 5c). By contrast, a significant increasing trend is seen in the nationwide ECW cluster after the transition year of 1987 (Figure 5b). The Qinghai–Tibetan Plateau ECW events decrease significantly during the study period with an overall trend of −0.21 per year (Figure 5d). From the perspective of the entire study period, decreasing trends are perceptible for all four clusters, which agrees with previous studies (Qian et al., 2019; Wang & Ding, 2006; Zhang & Qian, 2011; Zhou & Ren, 2010). However, the separation of the study period by years with an abrupt transition reveals an increasing trend in the occurrence number of nationwide ECWs since 1987.

3.2. Heat Budget Analysis

As speculated from the preceding section, diabatic heating may contribute to the cold SAT anomaly of the Qinghai-Tibetan Plateau ECW cluster. To illustrate this speculation, the heat budget is calculated at the near-surface 950 hPa level averaged during days -2–0 and within each cold anomaly center of the four clusters in Figure 4, which is conducive to the air temperature anomaly on the ECW day. Figure 6 displays the averaged 950 hPa air temperature anomaly tendency and relative contributions from different physical processes for the four ECW clusters. The cold temperature anomaly center is characterized by cold temperature anomaly tendency.

Considering the northeast ECW cluster (Figure 6a), the cold temperature tendency is contributed by most physical processes except adiabatic heating. The major contribution is by anomalous wind advecting climatological mean air temperature, and the second contribution is by the climatological mean flow advecting

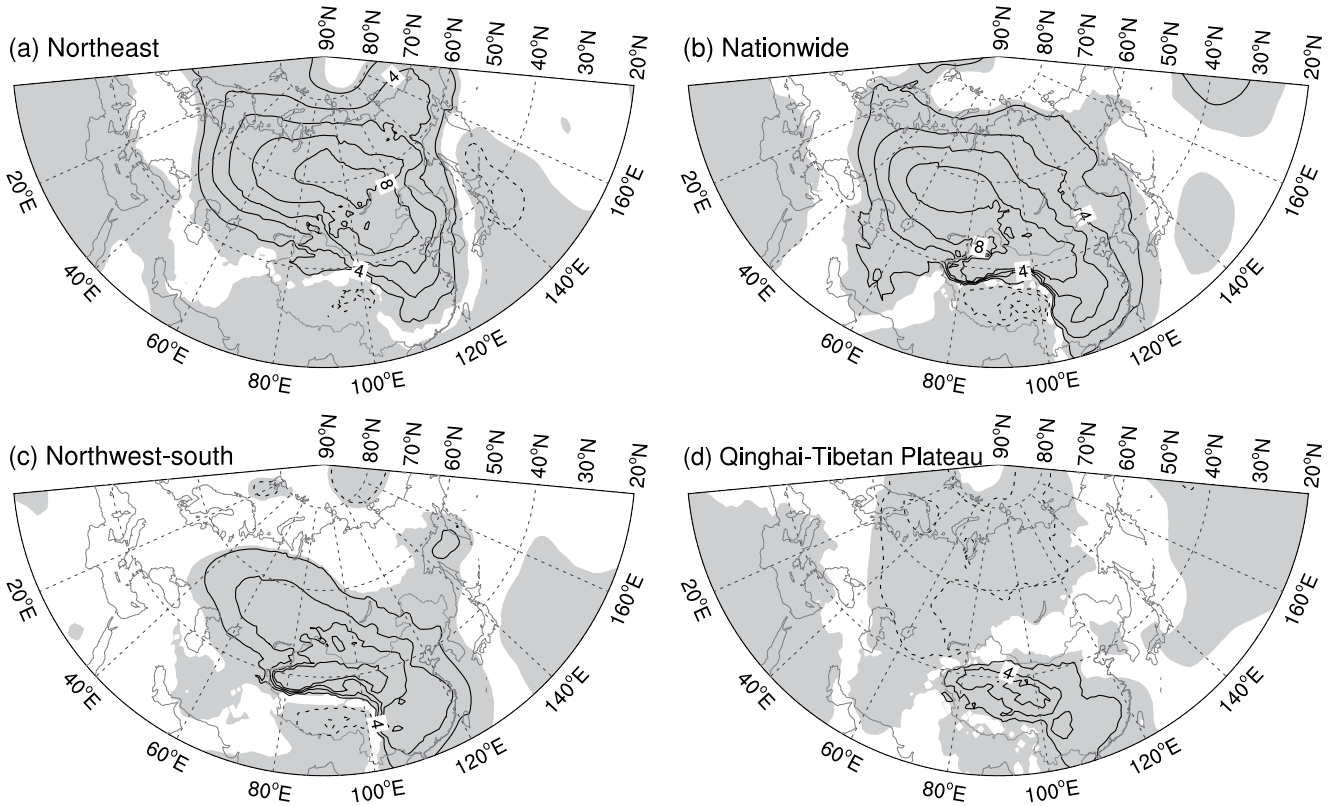

Figure 7. Composite SLP anomalies (contours; unit: hPa) for (a) the northeast extreme cold wave (ECW) cluster, (b) the nationwide ECW cluster, (c) the northwest–south ECW cluster and (d) the Qinghai–Tibetan Plateau ECW cluster. The contours are plotted for every 2 hPa and the shading represents the anomalies exceeding the 95% confidence level.

cold temperature anomaly. Unlike the other ECW clusters, the contributions by physical processes are larger than those of other ECW clusters and thus may result in the largest temperature anomaly tendency. In contrast, the nationwide and northeast-south ECW clusters are contributed by most physical processes except diabatic heating (Figures 6b and 6c). In addition, the nonlinear process provides a secondary contribution to the cold air temperature tendency. In comparison with the nationwide ECW cluster, the northeast-south ECW cluster receives minor contributions from climatological mean flow advecting cold temperature anomaly and adiabatic heating and stronger offsetting from diabatic heating. Considering the Qinghai-Tibetan Plateau ECW cluster (Figure 6d), as anticipated, the cold anomaly tendency is mainly contributed by the diabatic heating with secondary contribution from the anomalous horizontal wind advecting climatological-mean air temperature. The nonlinear processes provide a minor contribution to the cold air temperature tendency.

3.3. Circulation Features

Figure 7 shows the composite SLP anomalies that intimately regulate the SAT and wind anomalies for the four ECW clusters. Clusters 1–3 are characterized by an amplified Siberian high dominating over the Eurasian continent, with a southeastward extension along the lee side of Tibet to southern China, whereas cluster 4 features a dipole structure. The northeast ECWs are linked to a broad high SLP anomaly pattern that extends from the Arctic Ocean to eastern China, with a center over the north of Lake Baikal, which favors the incursion of robust cold SAT anomalies into Northeast China (Figures 4e and 7a). Compared with the northeast ECWs, the positive SLP anomaly of the nationwide ECWs shifts southwestward in a northwest–southeast orientation, with a center over the Sayan Mountains (Figure 7b). The positive SLP anomaly over China intensifies and extends southward along the lee side of Tibet to South China, inducing a more widespread cold SAT anomalies over China. The northwest–south ECWs are similar to the nationwide ECWs,

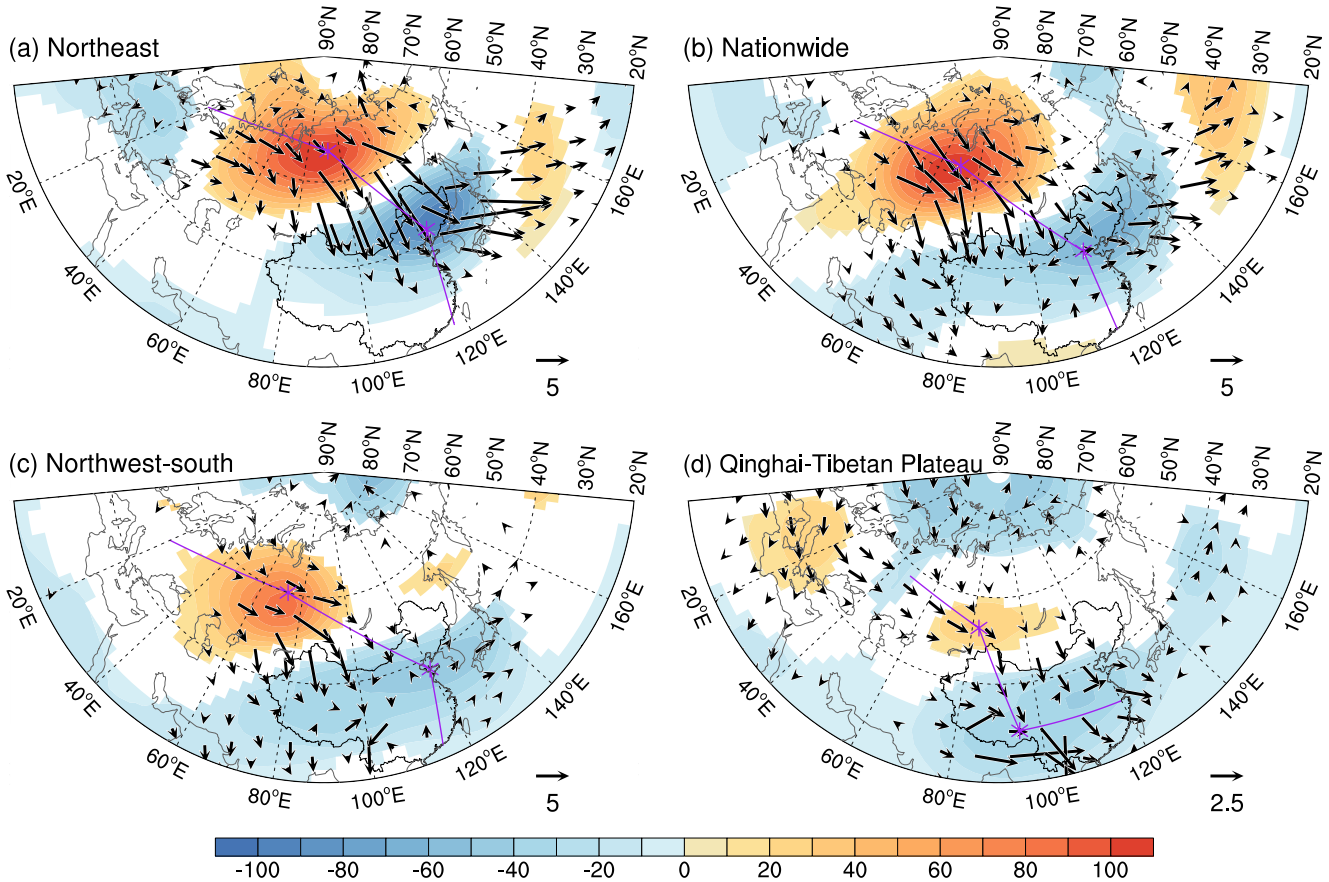

Figure 8. Composite Z500 anomalies (shading; unit: gpm) and wave activity fluxes (arrows; units: $m^2\ s^{-2}$) for (a) the northeast extreme cold wave (ECW) cluster, (b) the nationwide ECW cluster, (c) the northwest–south ECW cluster and (d) the Qinghai–Tibetan Plateau ECW cluster. Only composite anomalies that are statistically significant at the 95% confidence are shaded. Arrow magnitudes smaller than 2 and 0.5 $m^2\ s^{-2}$ are omitted in parts (a)–(c) and part (d), respectively, for clarity. The purple lines link anomalous centers (*) of the LMP for each cluster.

but with a smaller magnitude and a more regional distribution (Figure 7c). Therefore, the cold SAT is weaker than that of clusters 1–2. By contrast, the positive SLP anomaly for the Qinghai–Tibetan Plateau ECWs (Figure 7d) is confined to the region from Northwest China to Southeast China. Such a regional circulation is not capable of conveying cold air from higher latitudes (Figure 4h). To the north, a negative SLP anomaly dominates over the mid- and high-latitude Eurasian continent centered over the Scandinavian Peninsula.

The maintenance of near-surface circulations is coupled with the tropospheric circulations (Takaya & Nakamura, 2005; Xie, Black, & Deng, 2019), and thus, we show the composite Z500 anomalies and the corresponding Rossby wave activity flux for the four ECW groups in Figure 8. Similar to Xie et al. (2017a), we define the LMP as a composite Z500 anomaly pattern over the region (20°–90°N, 0°–180°E), which regulates the ECW events. The LMP is generally a dipole pattern over the Eurasian continent, with a positive height anomaly on the poleward side of a negative height anomaly, which is referred to as a pair of large-scale tilted ridges and troughs (Bueh et al., 2011; Bueh & Xie, 2015). The northeast ECWs feature a wave train from Europe to the North Pacific that encapsulates the dipole pattern, in which a significant positive height anomaly resides over Siberia with a center over the Yenisei river, and a negative height anomaly is zonally elongated from East Mongolia to Japan with a center over Northeast China. Rossby wave energy originating from Europe propagates southeastward through the positive anomaly over Siberia to the negative anomaly (Figure 8a). The dipole extends southwestward for the nationwide ECWs, particularly the negative height anomaly (Figure 8b). The positive height anomaly is tilted southwest–northeast and extends from the northern Arabian Peninsula to the Laptev Sea, with a center over the Ob river, whereas the negative height anomaly spans from the southern Arabian Peninsula to the Sea of Okhotsk with a center over the Bohai Sea. This agrees with the more southwestward extension of negative SAT anomalies in the nationwide ECWs than

the northeast ECWs. Meanwhile, broader Rossby wave energy is exported from the positive anomaly to the negative anomaly. Considering the northwest–south ECWs, the LMP migrates southward with a weaker magnitude (Figure 8c). Rossby wave energy propagation is more regional and confined to the region from the Ural Mountains to Northwest China. In contrast with the dipole pattern of clusters 1–3, the Qinghai–Tibetan Plateau ECWs are characterized by a weak positive height anomaly extending from Lake Balkhash to Northeast China, sandwiched between two negative anomalies over the Arctic Ocean and South China (Figure 8d). The propagation of Rossby wave energy is weaker than in clusters 1–3. This LMP is linked to the propagation of two different sources of Rossby wave energy from the Barents Sea and Europe, suggesting that the downstream components of the LMP are remotely forced.

Comparing the mid-tropospheric circulation with the SLP field shows that the positive anomaly of the LMP has an equivalent barotropic structure, whereas the negative anomaly has a baroclinic property. To combine the foregoing three circulation fields, Figure 9 shows cross-sections of the geopotential height anomaly and air temperature anomaly along the centers (maximum or minimum) of the Z500 anomalies for the four ECW clusters. The LMP is a deep system extending from the troposphere to the stratosphere, with centers around 300 hPa or the dynamic tropopause. The cold temperature anomalies extend from the surface to the dynamic tropopause and reside at the southeastern flank of the positive height anomaly. Considering clusters 1–3 (Figures 9a–9c), the positive height anomaly shows a barotropic structure with a southward extension in the lower troposphere, whereas the negative height anomaly shows a barotropic feature above the mid troposphere and a baroclinic signature in the lower troposphere. The baroclinic regions coincide with the cold temperature anomalies that are advected by the northerlies between the dipole. The cold cores are in concert with the Siberian high anomaly centers. In contrast with clusters 1–3, both the positive and negative anomalies of the Qinghai–Tibetan Plateau ECW cluster are characterized by a barotropic structure above the mid troposphere, with a baroclinic structure in the lower troposphere (Figure 9d). The cold anomaly between the dipole is the key region where the mid- and upper-tropospheric circulation and the near-surface circulation mutually intensify each other, resulting in ECWs (i.e., the baroclinic growth).

To illustrate the more dynamic aspects of the LMP, we adopted the potential temperature and horizontal winds on the 2-PVU surface (Figure 10). The propagation of Rossby wave energy in the mid and upper troposphere can be interpreted using the advection of potential vorticity associated with anomalous flows in the mid and upper troposphere (Evans & Black, 2003). The dynamic tropopause map retains the advantages of isentropic potential vorticity maps; in that, the potential temperature on the 2-PVU surface is also conserved following adiabatic and frictionless flow (Morgan & Nielsen-Gammon, 1998). The tropopause map condenses the 3D potential vorticity distribution onto a 2D map—that is, the potential vorticity on several isentropic surfaces can be seen simultaneously. Figure 9 shows that the dynamic tropopause is low (high) within the negative (positive) height anomaly and very steep in the jet stream, in agreement with the results of Morgan and Nielsen-Gammon (1998).

Compared with the composite Z500 anomaly field, the anomalous potential temperature on the 2-PVU surface features an additional zonally elongated positive anomaly band in the East Asian jet, and the negative anomaly confined to the north of the East Asian jet (Figure 10). The cold trough deepens toward the southwest from the semi-permanent East Asian cold trough via an anomalous westward cold advection. A moderate warm ridge and a closed low are seen over North Asia in the northeast ECWs (Figure 10a). The anomalous southerly and northeasterly winds to the west and southeast of the warm ridge induce the ridge to migrate westward, indicating that Rossby wave energy propagates southeastward to the closed low. The wind anomalies are mainly parallel with the potential temperature contours in the upper and middle reaches of the East Asian jet, suggesting an intensification of the jet. In contrast with the northeast ECWs, the nationwide ECWs feature a more pronounced warm ridge associated with more evident potential temperature advection, consisting with a stronger Rossby wave propagation (Figure 10b). Anomalous northeasterly winds prevail from the Laptev Sea via Mongolia to the Iranian Plateau, conveying the cold anomalies southwestward to form a broader cold trough. The broader cold advection corresponds to broader Rossby wave energy being exported from the warm ridge to the cold trough. The northwest–south ECWs resemble the nationwide ECWs, but the warm ridge is confined to western Siberia and the associated cold advection extends from the Sayan Mountains to the Aral Sea, where Rossby wave propagation is seen (Figure 10c). Similarly, the cold advection for the cold trough becomes more regional zonally from Japan to Lake Balkhash.

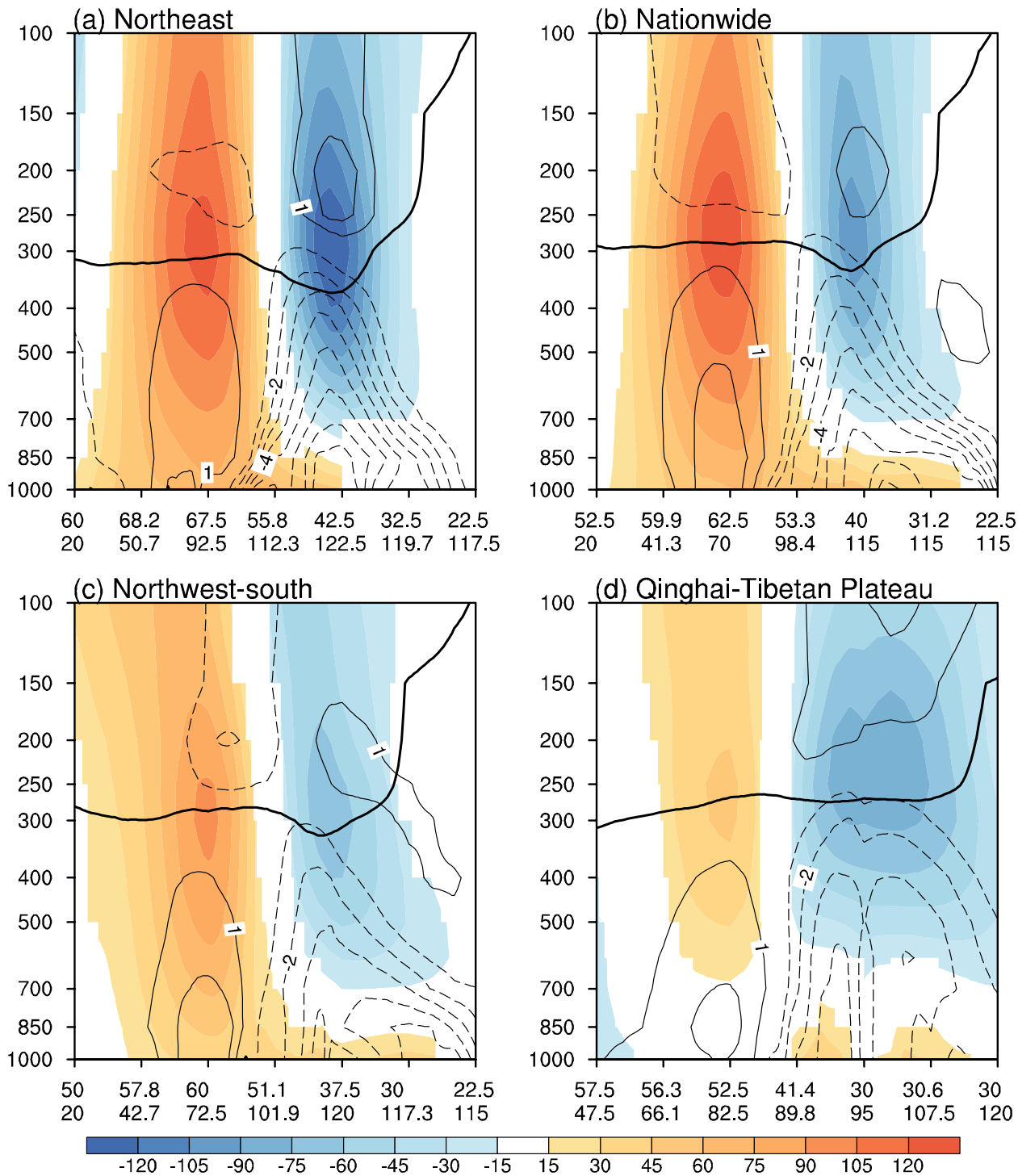

Figure 9. Composite cross-sections of geopotential height anomalies (shading; unit: gpm) and air temperature anomalies (contours; unit: °C) along the anomalous centers of the LMP for (a) the northeast extreme cold wave (ECW) cluster, (b) the nationwide ECW cluster, (c) the northwest–south ECW cluster and (d) the Qinghai–Tibetan Plateau ECW cluster. The labels on the *x*-axis are the latitudes and longitudes of the anomalous centers. The contours are plotted every 1°C and the zero lines are omitted. Only composite geopotential height anomalies that are statistically significant at the 95% confidence are shaded and the thick black contour is the 2-PVU contour of the composite potential vorticity.

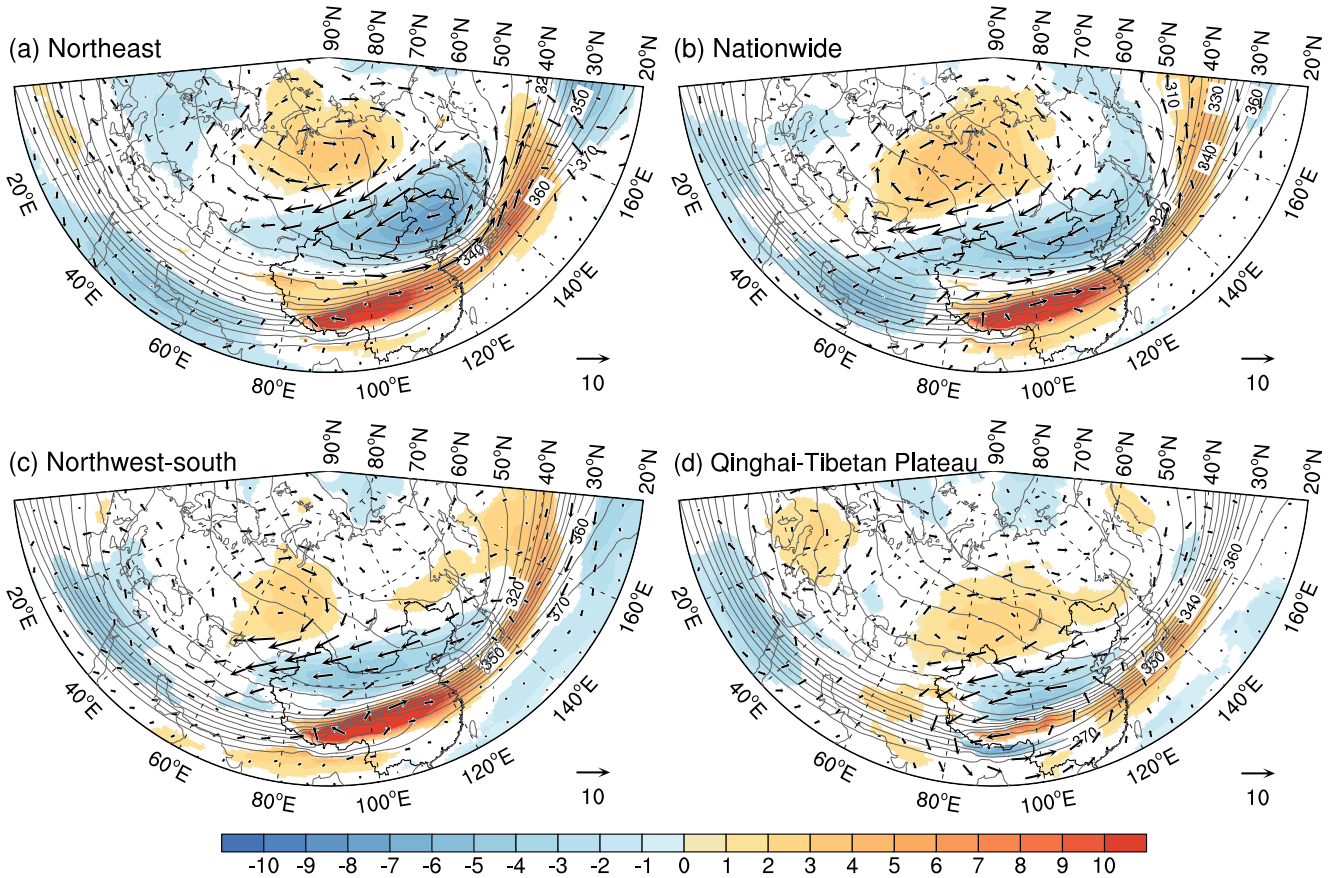

Figure 10. Composite 2-PVU potential temperature (contours; unit: K), potential temperature anomalies (shading; unit: K) and horizontal wind anomalies (arrows; units: m s^{-1}) for (a) the northeast extreme cold wave (ECW) cluster, (b) the nationwide ECW cluster, (c) the northwest–south ECW cluster and (d) the Qinghai–Tibetan Plateau ECW cluster. The contours are plotted every 5K Only composite anomalies that are statistically significant at the 95% confidence are shaded.

By contrast, the Qinghai–Tibetan ECWs are characterized by cold and warm advection that is distributed from Europe via Siberia to South China, suggesting remotely forced anomalies (Figure 10d). A moderate intensification of the East Asian jet is confined to the region from the coast of China to the North Pacific.

From the perspective of potential vorticity inversion, the circulation of the upper-tropospheric anomaly contributes greatly to the near-surface cold SAT advection (Takaya & Nakamura, 2005; Xie, Liu, et al., 2019). In turn, the cold SAT anomaly over the key region within the pair of warm ridges and troughs induces an anomalous anticyclonic flow that extends upward to the upper troposphere and advects low potential vorticity to the warm ridge and high potential vorticity to the cold trough (Bueh et al., 2018; Takaya & Nakamura, 2005; Xie, Liu, et al., 2019). This phase-locking between the upper-tropospheric LMP and the key lower-tropospheric region of the anomalous cold centers, also known as baroclinic instability, is an important contributor to ECWs.

4. Association With Planetary Waves

As mentioned above, studies have shown that the NAM modulates ECWs via synoptic weather systems (He, 2015; Park et al., 2011; Yuan & Li, 2019). Since the NAM index represents the total of anomalies, including the synoptic component, projecting onto the NAM pattern, the NAM pattern and synoptic weather system are not separated from each other in these studies. The preceding section emphasizes on the importance of baroclinic growth for the ECWs, which represents an interaction between anomalies and the mean flow. In this section, we separate the LMP into planetary- and synoptic-wave components to investigate the relationship between planetary wave patterns and LMPs for the ECWs.

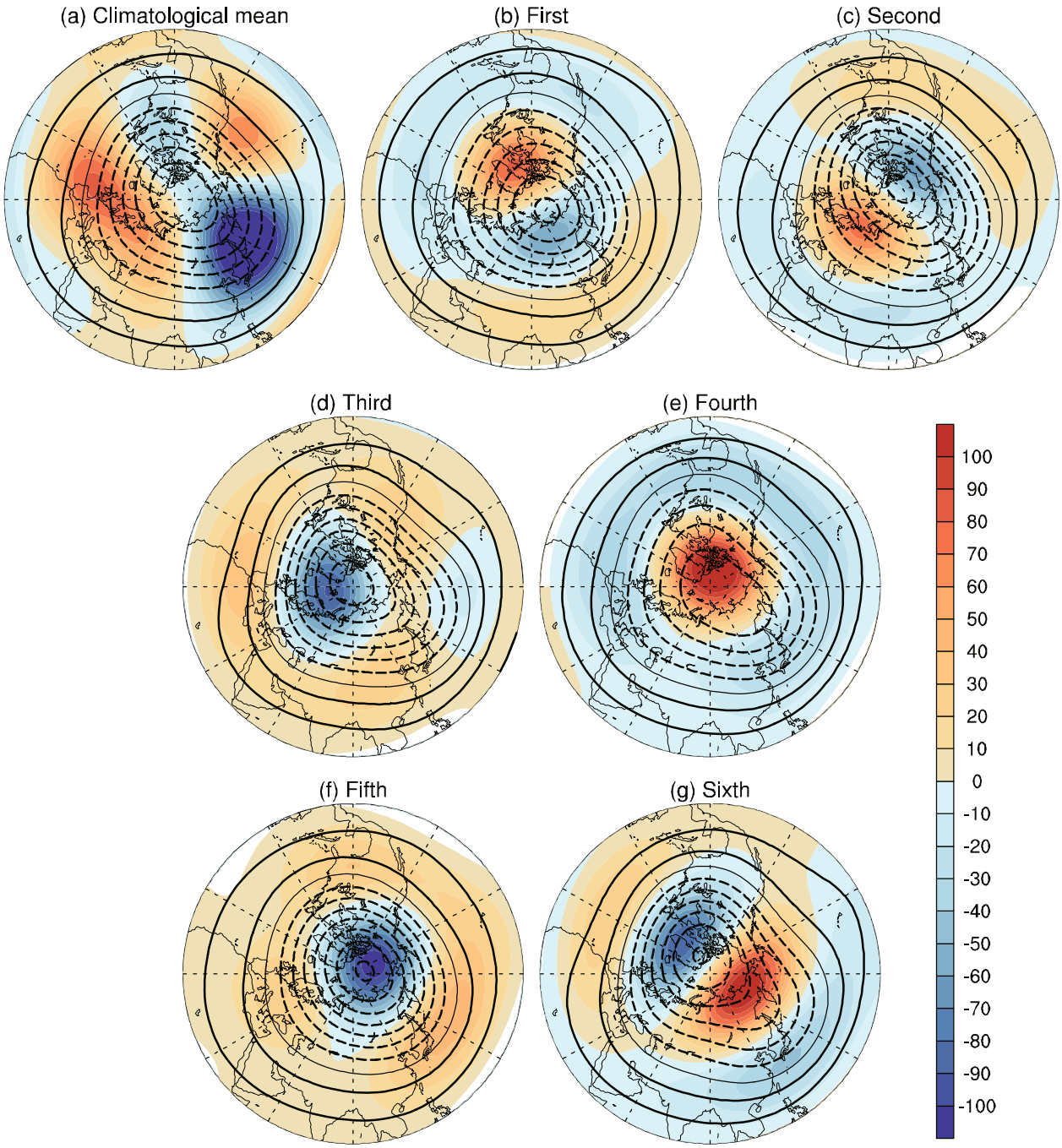

Figure 11. (a) Climatological mean Z500 of wave numbers 1–5 (contours; unit: gpm) and the corresponding latitudinal deviation field (shading; replotted from Xie et al. (2017b)). The composite Z500 of wave numbers 1–5 (contours) and the corresponding anomalies relative to the climatological mean (shading) for the (b) first, (c) second, (d) third, (e) fourth, (f) fifth and (g) sixth planetary wave patterns. The contours are drawn every 100 gpm, the solid (dashed) lines represent the positive (negative) Z500 of wave numbers 1–5 and the thin lines indicate zero. Only composite anomalies that are statistically significant at 95% confidence interval are shaded. The lowest point in each panel is drawn at (90°E, 10°N).

In concert with Figure 2 of Xie et al. (2017b), Figure 11 shows composite Z500 of wavenumbers 1–5 and the corresponding anomalies relative to the climatological mean for six planetary wave patterns from the ERA reanalysis during the period 1961–2015. Climatologically, the stationary wave ridges and troughs alternately reside over the eastern portions of the oceans and continents (Figures 11a). The six planetary wave patterns are identical to those of Xie et al. (2017b). The first (sixth) pattern combines the positive (negative) phase

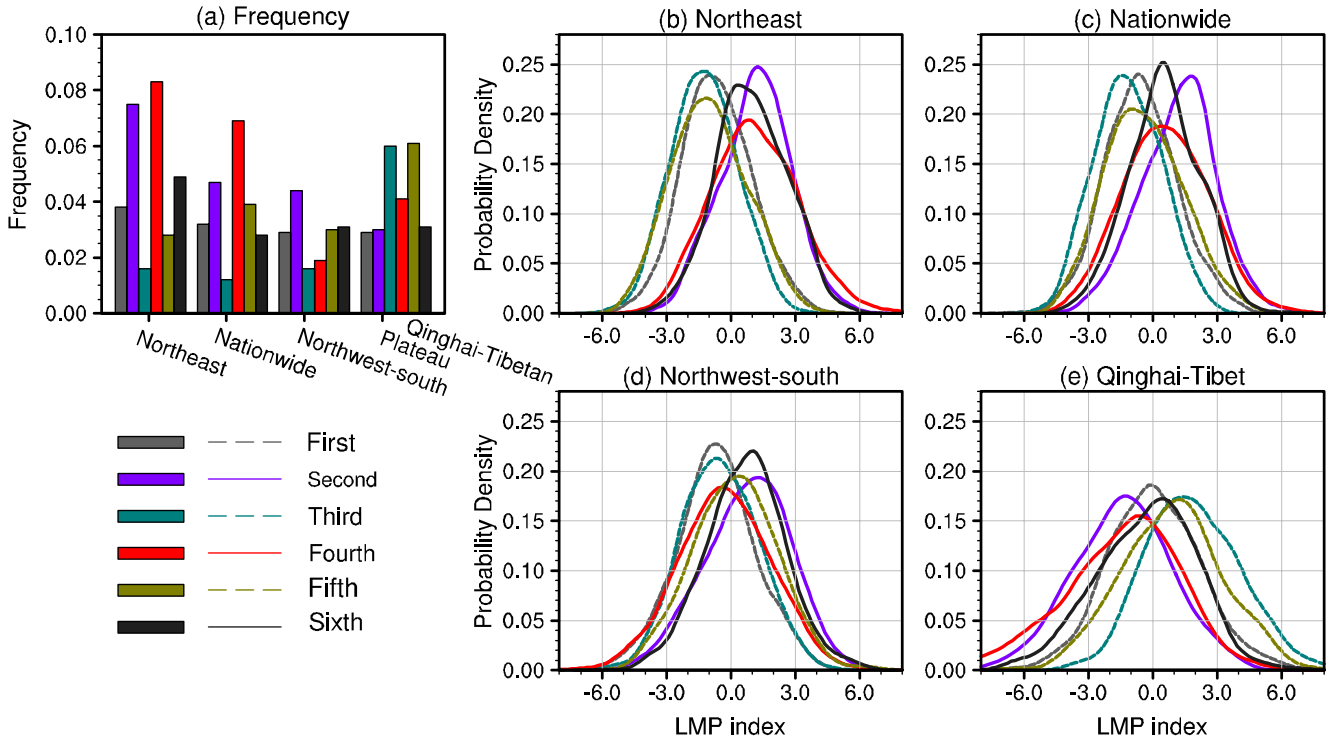

Figure 12. (a) Frequency of days of each planetary wave pattern with each extreme cold wave (ECW) cluster occupied on the total number days of the corresponding planetary waves. Probability density function (PDF) of the LMP index of each planetary wave for (b) the northeast ECW cluster, (c) the nationwide ECW cluster, (d) the northwest–south ECW cluster and (e) the Qinghai–Tibetan Plateau ECW cluster.

of the Pacific/North American teleconnection pattern and the negative (positive) phase of the West Pacific pattern (Figures 11b and 11g; Xie, Black, & Deng, 2019). The second pattern represents an amplification of the climatological mean planetary waves (Figures 11c). The fourth and fifth patterns are antisymmetric to each other and resemble the negative and positive phases of the NAM, respectively (Figures 11e and 11f). The third planetary wave pattern is similar to the fifth pattern, but with a negative height anomaly over the Greenland Sea.

To explore the relationship between ECWs and the planetary wave patterns, we construct an LMP index and calculate the ECW occurrence frequencies and corresponding LMP index probability density function (PDF) stratified by the six planetary wave patterns. Following the approach of Xie et al. (2017a), a daily LMP index is constructed by projecting each daily Z500 anomaly pattern (Z') on each LMP (Z'_{LMP}) using a pattern amplitude projection (Deng et al., 2012):

$$\text{LMP index} = \frac{A^{-1}\int_A a^2 Z' Z'_{\text{LMP}} \cos\varphi d\lambda d\phi}{A^{-1}\int_A a^2 \left(Z'_{\text{LMP}}\right)^2 \cos\varphi d\lambda d\phi}, \quad (3)$$

where A represents the area of the LMP (10°–85°N, 0°–180°E), a is the mean radius of the Earth, and λ and ϕ are the longitude and latitude, respectively. This LMP index measures both the LMP phase and amplitude at the same time (Xie at al., 2017a).

Figure 12 shows the occurrence frequency of ECWs (Figure 12a) together with the PDFs of the corresponding ECW LMP indices (Figures 12b–12e), all stratified in terms of the six planetary wave patterns. The frequency is defined as a fraction of the total number of days in which a specific planetary wave pattern occurs, that is, $f(i,j) = n(i,j)/N(j)$, where $N(j)$ is the total number of days associated with the jth planetary wave pattern and $n(i,j)$ is the number of days that the ith ECW cluster is concurrent with the jth planetary wave pattern. As expected, clusters 1 and 2 tend to be more frequent during episodes of the second and fourth planetary wave patterns, particularly the fourth planetary wave pattern (Figure 12a), whereas the

northwest–south ECWs are most frequent during the second planetary wave period. This is consistent with Xie et al. (2017b), which noted that the second and fourth planetary wave patterns favor cold SAT anomalies over the Chinese mainland. These two planetary wave patterns overlap with the LMPs of clusters 1–3, particularly the negative height anomalies over China (Figures 8a–8c). By contrast, the Qinghai–Tibetan Plateaus ECWs are preferentially favored during the third and fifth planetary wave episodes.

The presence of planetary wave patterns also strongly affects the probability distributions of the ECW LMPs, which provide the organizing regional large-scale circulation for ECWs. The northeast- and nationwide ECW LMPs are more frequent (right-shifted PDFs) in association with the second and fourth patterns, suggesting that both of these planetary wave patterns favor the occurrence of the LMPs responsible for northeast- and nationwide ECW clusters (Figures 12b and 12c). By contrast, the LMPs are less frequent (left-shifted PDFs) in association with the first, third and fifth planetary wave patterns, which are out of phase with the LMP. For the northwest–south ECWs, the LMP distribution is most strongly affected by the second planetary wave pattern, which corresponds well with the impact of the second planetary wave pattern on the occurrence frequency of ECWs (Figures 12a and 12d). Comparing the structures of the LMPs (Figure 8c) with the second planetary wave pattern (Figures 11c), the anomalies are in phase with each other. In contrast with the ECW clusters 1–3, the PDF for the Qinghai–Tibetan Plateau ECW LMPs is right-shifted during days with the third and fifth planetary wave patterns, indicating that the positive phase of the NAM favors the occurrence of the Qinghai–Tibetan Plateau ECW cluster. The LMP structure of the Qinghai–Tibetan Plateau ECW cluster overlaps with the third and fifth planetary wave patterns over mid and high latitudes (Figures 8d, 11d and 11f).

Because both the planetary and synoptic waves constitute the daily LMP of ECWs, we decompose the daily LMP into planetary and synoptic components to evaluate each separate contribution to the daily LMP. The contributions of planetary and synoptic components to the daily LMP are quantified using a pattern amplitude projection (Deng et al., 2012). The calculation is same as Equation 3, except that Z' is replaced by the planetary and synoptic components of daily Z'_{LMP}, which indicates the contributions from planetary and synoptic to the daily LMP, respectively. The planetary component of Z'_{LMP} is derived as wavenumbers 1–5 using the spherical harmonic decomposition, while the remainder of Z'_{LMP} is considered as the synoptic component. The sum of the planetary and synoptic projection indices is equal to 1 and therefore Figure 13 only shows the PDFs of the planetary projection indices stratified in terms of the favorable planetary wave patterns for the four ECW clusters. The average planetary projection indices are about 0.33, 0.32, 0.35, and 0.32 for the four ECW clusters, respectively.

The fourth planetary wave contributes more (right-skewed PDF) to the LMP than the other planetary waves for the northeast and nationwide ECWs (Figures 13a and 13b), which agrees with the resemblance between their LMPs and the fourth planetary wave pattern, particularly the negative height anomaly extending from the North Pacific to central Asia. The right-skewed PDF of the second planetary wave is only seen in the nationwide ECWs among ECW clusters 1–3 (Figures 13a–13c), in which the nationwide ECW LMP is more in phase with the second planetary wave pattern (Figures 8b and 11c) than the northeast and northwest–south ECW LMPs. Unlike the fourth planetary wave, the contribution of the second planetary wave pattern relies more heavily on the positive height anomaly over the northern Eurasian continent. Such a positive height anomaly overlaps with the negative height anomalies of the northeast ECW LMP (Figures 8a and 11c), resulting in a smaller contribution than that from other planetary waves (Figure 13a). The northwest–south ECW LMP displaces southward with respect to the second planetary wave pattern and thus receives a smaller contribution from this planetary wave pattern. Considering the Qinghai–Tibetan Plateau ECWs, the PDF is right-skewed during days influenced by the third planetary wave pattern and bimodal with a new peak around 0.65 during the days influenced by the fifth planetary wave pattern (Figure 13d). Inspection of Figures 11d and 11f shows that the regional circulation of the third planetary wave pattern over Eurasia and the Arctic is displaced further west than that of the fifth planetary wave, which yields a greater contribution to the Qinghai–Tibet Plateau ECW LMP.

The planetary waves not only contribute directly to the ECW LMP but also provide a favorable background for the baroclinic growth of synoptic waves. Here, we choose the typical nationwide ECWs, which are most influential over the Chinese mainland and intimately associated with the second and fourth planetary wave patterns, to investigate the baroclinic growth during periods associated with different planetary wave patterns.

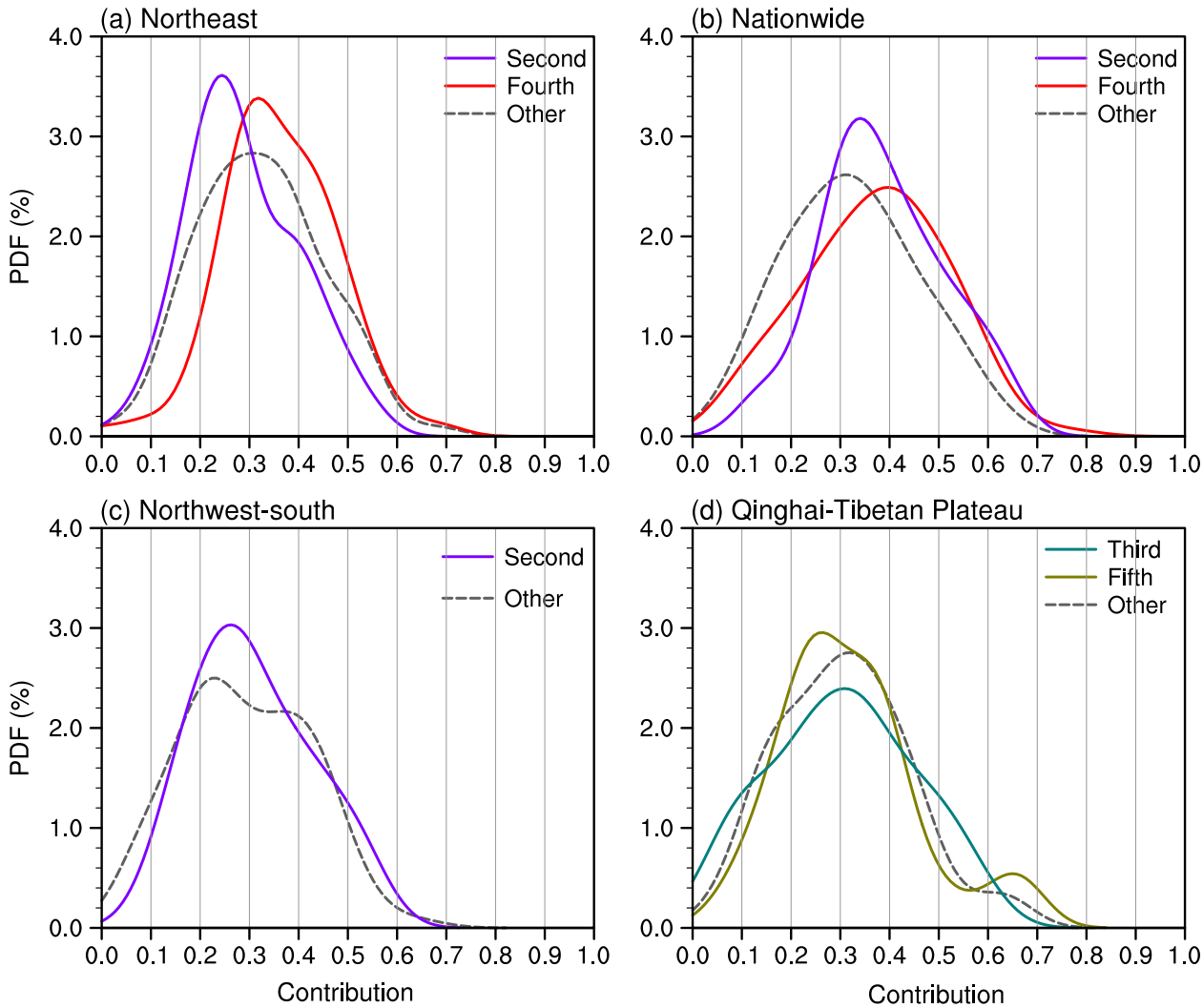

Figure 13. Probability density function (PDF) of the contributions of planetary waves to the LMP for (a) the northeast extreme cold wave (ECW) cluster, (b) the nationwide ECW cluster, (c) the northwest–south ECW cluster and (d) the Qinghai–Tibetan Plateau ECW cluster.

We adopt the baroclinic conversion given by Robinson and Black (2005):$-u't' * \left(\partial\overline{T}/\partial x\right) - v't' * \left(\partial\overline{T}/\partial y\right)$. The prime denotes the synoptic waves, while the overbar denotes the planetary waves. The positive value of the baroclinic conversion indicates that the energy is converted from the planetary waves to the synoptic waves, which suggests that the planetary waves act as background circulation sustain the baroclinic growth of synoptic waves. The vertical profile of composite baroclinic energy conversion between the dipole of the LMP shows the largest value at 700 hPa (Figure S2 in supplement). Therefore, we choose 700 hPa level to display the composite baroclinic energy conversion during periods associated with the second, fourth, and other planetary wave patterns in Figure 14.

As anticipated, there are evident baroclinic energy conversions from background fields to LMPs over the region extending from southwestern Siberia to Northeast China (Figure 14). In comparison with other planetary wave patterns (Figure 14c), the LMPs during the periods of the second and fourth planetary wave patterns are associated with more apparent baroclinic energy conversion (Figures 14a and 14b). Similarly, the northeast- and northwest-south ECW LMPs receive a larger baroclinic energy conversion during the periods associated with the second planetary waves (Figures S3 and S4).

Since the second and fourth planetary wave patterns not only contribute more to the nationwide ECW LMP but also increase the baroclinic energy conversion to sustain the LMP, the decadal variability of the

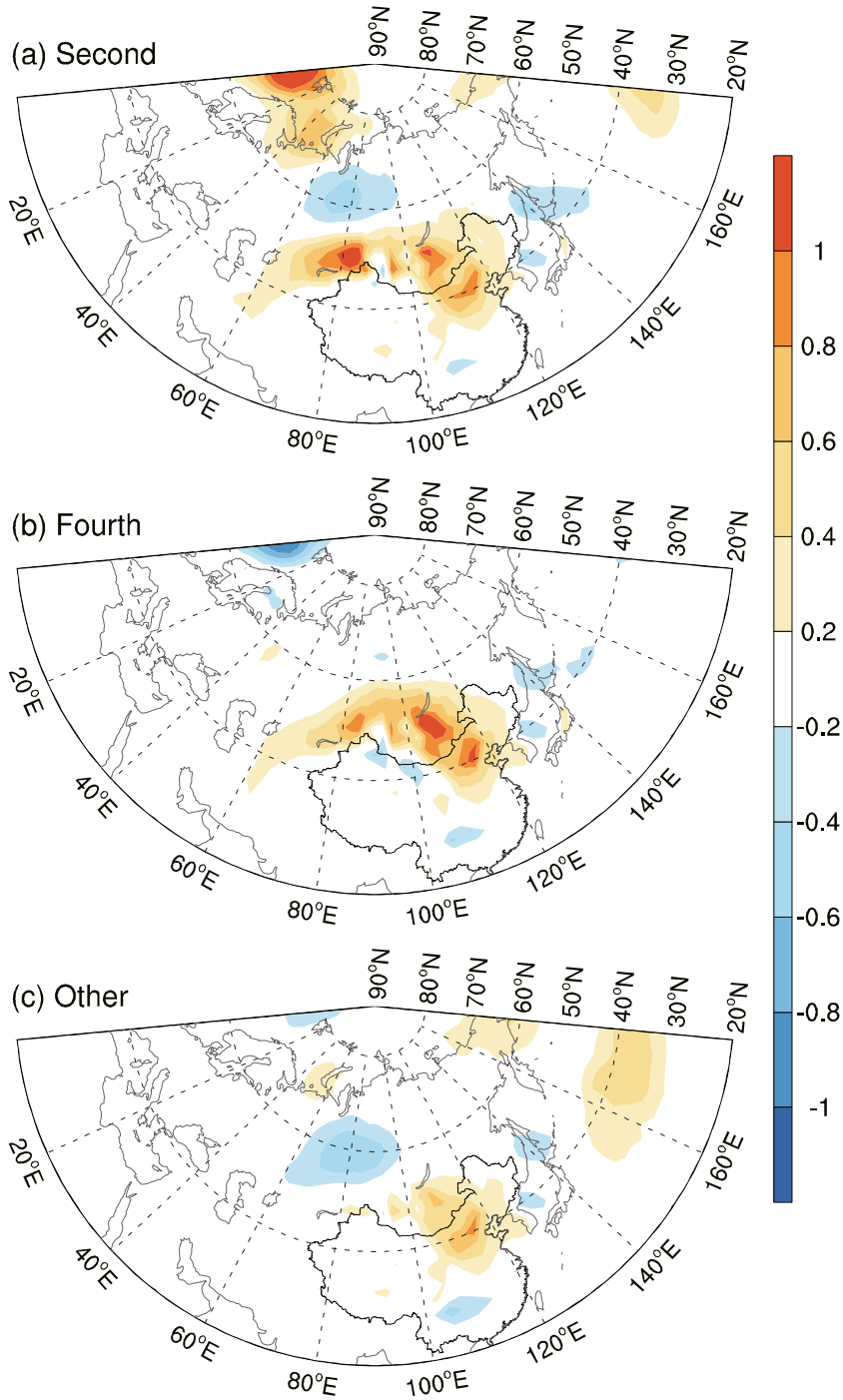

Figure 14. Composite 700 hPa baroclinic energy conversion (shading, units: 10^{-4} K^2 s^{-1}) of the nationwide extreme cold wave (ECW) cluster during periods associated with the (a) second, (b) fourth and (c) other planetary wave patterns.

nationwide ECWs may be modulated by these two planetary waves. Figure 15 displays time series of the annual occurrence number for the second and fourth planetary wave patterns and the derived trend lines during two subperiods separated by 1987. There are increasing trends for two planetary waves during the period over 1987–2015, particularly for the fourth planetary wave pattern. The trend of the fourth planetary wave pattern is 0.67 days y^{-1} and is significant at the 91% confidence level. Thus, the increasing trend of the nationwide ECWs during the period 1987–2015 is possibly associated with the positive trends of the second and fourth planetary wave patterns, particularly the latter.

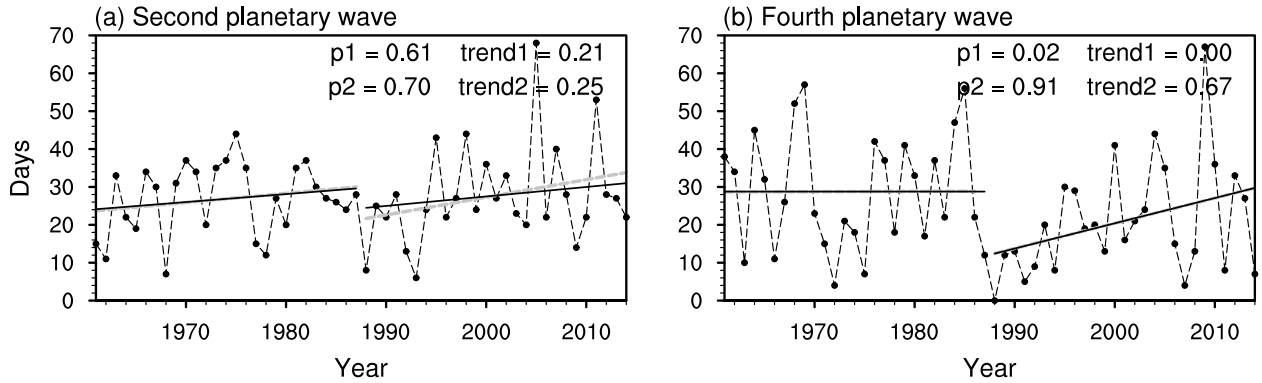

Figure 15. Same as Figure 5, but for (a) the second planetary wave pattern and (b) the fourth planetary wave pattern.

5. Summary and Discussion

We systematically investigated different ECW patterns over the Chinese mainland and their associated intraseasonal circulation features during the boreal cold season (November to March) for the period 1961–2015. The LMP for each ECW cluster was defined in terms of the composite *daily* Z500 anomalies, and the associated dynamics were tentatively interpreted from a potential vorticity advection perspective. We also examined the linkages between ECW LMPs and daily planetary wave patterns.

The ECW events were grouped into four distinct ECW patterns with cold SAT anomalies displacing southwestward from Northeast China to West China. According to the geographical distributions of the cold SAT anomalies, four ECW clusters were identified: northeast ECWs, nationwide ECWs, northwest–south ECWs, and Qinghai–Tibetan Plateau ECWs. The annual occurrence numbers of the ECW clusters 1–3 are characterized by significant transitions in the years 1990, 1987, and 1992, respectively. There are decreasing trends for the northeast and northwest–south ECWs prior to the transition years, whereas a significant increasing trend is seen for the nationwide ECWs after the transition year. By contrast, the Qinghai–Tibetan Plateau ECW events show a pronounced decreasing trend over the entire period. The cold anomalies of the leading three ECW clusters are mainly contributed by the anomalous wind advecting climatological mean flow, while that of the Qinghai–Tibetan Plateau ECW is contributed by the diabatic heating.

The LMPs are primarily characterized by a dipole with a southwest–northeast tilt, which favors their baroclinic growth. The ECW clusters 1–3 feature a positive height anomaly over Siberia and a negative height anomaly elongated zonally from Japan to the Iranian Plateau, whereas the Qinghai–Tibetan Plateau ECW cluster shows a wave train over the Eurasian continent. The LMP has an equivalent barotropic structure, with the largest amplitude around 300 hPa or the dynamic tropopause, in which the negative height anomaly has a baroclinic signature in the lower troposphere. Such a baroclinic region between the anomalies of the dipole is the key region to maintain the LMP. The LMPs induce anomalous northerly flows extending from the upper troposphere to the near-surface. The northerly flows deepen the negative height anomaly southwestward from the semi-permanent East Asian trough and accumulates cold air masses over the key region between the anomalies of the dipole, which are phase-locked with the tropospheric LMPs (i.e., baroclinic growth). It could be concluded that Rossby wave energy triggers the LMP over the key region and then favors baroclinic growth of the LMP that produces extremes.

The ECW events tend to occur during the periods associated with a favorable planetary background circulation with more contributions to the LMPs than other planetary waves. The fourth planetary wave, which resembles the negative phase of the NAM, increases the probability of the northeast- and nationwide ECW LMPs and thus the occurrence of ECW events via more direct contributions to the LMPs. The second planetary wave pattern, representing an amplification of the climatological mean, favors the occurrence of the ECW clusters 1–3 via increasing the baroclinic growth of their LMPs. In addition, the second planetary wave also provides more direct contribution to the nationwide ECW LMP. After the transition year of 1987, these two planetary waves, particularly the fourth planetary wave, exhibit a positive trend and thus are likely to increase the occurrence of the nationwide ECWs. The Qinghai–Tibetan Plateau ECW cluster is

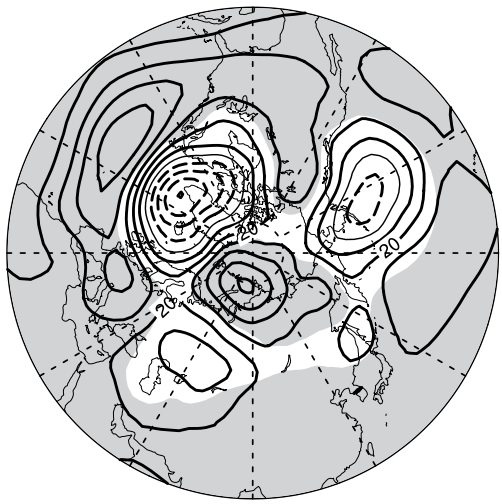

Figure 16. The spatial distribution of linear trend (contour, units: gpm yr^{-1}) of Z500 during the boreal season over 1961–2014. Shading represents the trend exceeding the 95% confidence level and the thin lines indicate zero.

more frequent during the periods associated with the third and fifth planetary waves, which increase the probability of the LMP by contributing more directly to the LMP than the other planetary waves. Compared with earlier studies, which used a daily teleconnections index including both planetary and synoptic waves, we decomposed the daily LMP into planetary and synoptic components and isolated the contribution of planetary waves to the LMP.

The consecutive spatial structure of the four ECW clusters suggests a potential connection among them. We simply counted the number of each cluster followed by its subsequent cluster during an ECW event to address this concern. Most ECW events remain in the same cluster with 81.2%, 71.4%, 62.0%, and 88.9% of the total number of ECW days for clusters 1–4. There are 13.4%, 18.5%, and 23.2% of ECW days followed by the subsequent clusters for clusters 1–3. The result indicates that these three clusters have some associations with different stages of a developing ECW that starts over the northeast and then eventually expands southward and southwestward.

To illustrate whether there is a significant difference between the nationwide and northwest-south ECW clusters, we calculated the differences of circulations between them (Figure S5). As seen from Figure S5, the differences of SAT, SLP, and Z500 fields are significant between these two ECW clusters. Compared to the northwest-south ECW clusters, the nationwide ECW cluster features more conspicuous cold SAT anomaly over eastern China, particularly northeastern China. The SLP also shows more extensive and intensive over Siberia for the nationwide ECW cluster. Similarly, the wave train of Z500 for the nationwide ECW cluster is more pronounced than the northwest-south ECW cluster. Therefore, circulations of the northwest-south ECW cluster exhibit a more regional feature than the nationwide ECW cluster. Therefore, the northwest-south ECW cluster possibly outbreaks from northwest China southeastward to south China. In comparison, the nationwide ECW cluster engulfs the Chinese mainland that is maintained by more extensive and intensive circulations. Therefore, we consider that they could not be merged together.

The temperature warming trend is increased with altitude and is strongest during the boreal cold season in the Qinghai-Tibetan Plateau (Liu et al., 2006), which may lead to an increase of Z500 in situ (Duan & Wu, 2009) and a reduced occurrence frequency of ECW. Gong et al. (2021) noted that the decline of autumn Arctic sea ice associated with the global warming can induce a positive SAT trend over the Tibetan Plateau. Thus, we speculated that the warming pattern in the Northern Hemisphere could lead to a significant decrease in the occurrence number of Qinghai-Tibetan Plateau ECW cluster since 1961. Figure 16 shows the linear trend of Z500 during the boreal cold season from 1961–2014 in the Northern Hemisphere, which could be attributable to the global warming via an optimal fingerprinting regression (Christidis & Stott, 2015). The linear trend of Z500 features an overall positive trend in the Northern Hemisphere with significant positive anomalies in the Arctic and the low-mid latitudes. Such positive trends are antisymmetric with the LMP of the Qinghai-Tibetan Plateau ECW cluster, which shows negative height anomalies in the Arctic and China (Figure 8). Therefore, the significant decrease in the occurrence number of Qinghai-Tibetan Plateau ECW events since 1961 could be attributable to the Northern Hemisphere warming pattern. However, the physical mechanism in detail needs a further investigation. Considering the planetary wave defined in current paper, we removed the total wavenumber 0, which represent the areal mean of Z500 in the Northern Hemisphere. Therefore, the overall warming is subtracted from the daily planetary wave, and no significant trend is seen in the third and fifth planetary waves.

We investigated the dynamic aspect of LMPs from a potential vorticity advection perspective; more detailed dynamic processes, including barotropic and nonlinear processes, will be quantified in future studies based on the lifecycle features. Although there is a direct contribution of planetary waves favoring ECWs to the LMPs, the majority of the contribution is from the synoptic wave (Cheung, Zhou, Mok, et al., 2013; Zhou

et al., 2009). The question of how planetary waves change the background circulation that promotes the growth of synoptic LMPs will be addressed in future studies.

Data Availability Statement

The APHRODITE daily gridded surface air temperature data were obtained from the Hirosaki University, https://www.chikyu.ac.jp/precip/english/downloads.html. The EAR40 and ERA5 reanalysis data were derived from https://apps.ecmwf.int/datasets/data/era40-daily/levtype=sfc/ and https://cds.climate.copernicus.eu/cdsapp#!/dataset/reanalysis-era5-pressure-levels?tab=overview, respectively.

Acknowledgments
We thank three anonymous reviewers for their constructive comments and suggestions. This research was funded by the National Natural Science Foundation of China (41875078, 42005033 & 41861144014) and the National Key Research and Development Program of China (2016YFA0601501). Yi Deng is in part supported by the U.S. National Science Foundation (NSF) through Grant AGS-2032532 and by the U.S. National Oceanic and Atmospheric Administration (NOAA) through Grant NA20OAR4310380.

References

Bueh, C., Peng, J., Lin, D., & Chen, B. (2021). On the two successive supercold waves straddling the end of 2020 and the beginning of 2021. *Advances in Atmospheric Sciences*. https://doi.org/10.1007/s00376-021-1107-x

Bueh, C., Peng, J., Xie, Z., & Ji, L. (2018). Recent progresses on the studies of wintertime extensive and persistent extreme cold events in China and large-scale titled ridges and troughs over the Eurasian Continent (in Chinese). *Chinese Journal of Atmospheric Sciences*, *42*(3), 656–676. https://doi.org/10.3878/j.issn.1006-9895.1712.17249

Bueh, C., Peng, J., Xie, Z., & Shi, N. (2015). *A study in extensive persistent extreme cold event in China during winter (in Chinese)* (pp. 1–230). China Meteorological Press.

Bueh, C., Shi, N., & Xie, Z. (2011). Large-scale circulation on anomalies associated with persistent low temperature over southern China in January 2008. *Atmospheric Science Letters*, *12*(3), 273–280. https://doi.org/10.1002/asl.333

Bueh, C., & Xie, Z. (2015). An objective technique for detecting large-scale tilted ridges and troughs and its application to an East Asian cold event. *Monthly Weather Review*, *143*(12), 4765–4783. https://doi.org/10.1175/MWR-D-14-00238.1

Chen, W., & Kang, L. H. (2006). Linkage between the Arctic Oscillation and winter climate over East Asia on the interannual timescale: Roles of quasi-stationary planetary waves (in Chinese). *Chinese Journal of Atmospheric Science*, *30*(5), 863–870.

Cheung, H. N., Zhou, W., Mok, H. Y., & Wu, M. C. (2012). Relationship between Ural-Siberian blocking and the East Asian winter monsoon in relation to the Arctic Oscillation and the El Niño-Southern Oscillation. *Journal of Climate*, *25*(12), 4242–4257. https://doi.org/10.1175/JCLI-D-11-00225.1

Cheung, H. N., Zhou, W., Mok, H. Y., Wu, M. C., & Shao, Y. (2013). Revisiting the climatology of atmospheric blocking in the Northern Hemisphere. *Advances in Atmospheric Sciences*, *30*(2), 397–410. https://doi.org/10.1007/s00376-012-2006-y

Cheung, H. N., Zhou, W., Shao, Y., Chen, W., Mok, H. Y., & Wu, M. C. (2013). Observational climatology and characteristics of wintertime atmospheric blocking over Ural–Siberia. *Climate Dynamics*, *41*, 63–79. https://doi.org/10.1007/s00382-012-1587-6

Christidis, N., & Scott, P. A. (2015). Changes in the geopotential height at 500 hPa under the influence of external climatic forcing. *Geophysical Research Letters*, *42*, 10798–10810. https://doi.org/10.1002/2015GL066669

Deng, J., Dai, A., & Chyi, D. (2020). Northern Hemisphere winter air temperature patterns and their associated atmospheric and ocean conditions. *Journal of Climate*, *33*(14), 6165–6186. https://doi.org/10.1175/JCLI-D-19-0533.1

Deng, Y., Park, T. W., & Cai, M. (2012). Process-based decomposition of the global surface temperature response to El Nino in boreal winter. *Journal of Atmospheric Science*, *69*(5), 1706–1712. https://doi.org/10.1175/JAS-D-12-023.1

Ding, Z., Li, L. J., Wei, R. Q., Dong, W. Y., Guo, P., Yang, S. Y., et al. (2016). Association of cold temperature and mortality and effect modification in the subtropical plateau monsoon climate of Yuxi, China. *Environmental Research*, *150*, 431–437. https://doi.org/10.1016/j.envres.2016.06.029

Duan, A., & Wu, G. (2009). Weakening trend in the atmospheric heat source over the Tibetan Plateau during recent decades. Part II: Connection with climate warming. *Journal of Climate*, *22*, 4197–4212. https://doi.org/10.1175/2009JCLI2699.1

Evans, K. J., & Black, R. X. (2003). Piecewise tendency diagnosis of weather regime transitions. *Journal of Atmospheric Science*, *60*(16), 1941–1959. https://doi.org/10.1175/1520-0469(2003)060<1941:PTDOWR>2.0.CO;2

Fu, C., & Wang, Q. (1992). The definition and detection of the abrupt climatic change (in Chinese). *Chinese of Journal Atmospheric Science*, *16*(4), 482–493.

Gong, D. Y., Wang, S. W., & Zhu, J. H. (2001). East Asian winter monsoon and Arctic Oscillation. *Geophysical Research Letters*, *28*, 2073–2076. https://doi.org/10.1029/2000GL012311

Gong, H., Wang, L., Chen, W., & Wu, R. (2021). Evolution of the East Asian winter land temperature trends during 1961-2018: Role of internal variability and external forcing. *Environmental Research Letters*, *16*(2), 024015. https://doi.org/10.1088/1748-9326/abd586

Grotjahn, R., Black, R., Leung, R., Wehner, M. F., Barlow, M., Bosilovich, M., et al. (2016). North American extreme temperature events and related large scale meteorological patterns: A review of statistical methods, dynamics, modeling, and trends. *Climate Dynamics*, *46*, 1151–1184. https://doi.org/10.1007/s00382-015-2638-6

He, J., & Black, R. X. (2016). Heat budget analysis of Northern Hemisphere high-latitude spring onset events. *Journal of Geophysical Research Atmosphere*, *121*, 10113–10137. https://doi.org/10.1002/2015jd024681

He, S. P. (2015). Asymmetry in the Arctic Oscillation teleconnection with January cold extremes in Northeast China. *Atmospheric and Oceanic Science Letters*, *8*(6), 386–391. https://doi.org/10.3878/AOSL20150053

Hersbach, H., Bell, B., Berrisford, P., Hirahara, S., Horanyi, A., et al. (2020). The ERA5 global reanalysis. *Quarterly Journal of the Royal Meteorological Society*, *146*(730), 1999–2049. https://doi.org/10.1002/qj.3803

Hou, Y. P., Zhang, M. F., Liu, S. R., Sun, P. S., Yin, L. H., Yang, T., et al. (2018). The hydrological impact of extreme weather-induced forest disturbances in a tropical experimental watershed in south China. *Forests*, *9*(12), 734. https://doi.org/10.3390/f9120734

Hyndman, R. J., & Fan, Y. (1996). Sample quantiles in statistical package. *The American Statistician*, *50*(4), 361–365. https://doi.org/10.1080/00031305.1996.10473566

Jeong, J. H., & Ho, C. H. (2005). Changes in occurrence of cold surges over east Asia in association with Arctic Oscillation. *Geophysical Research Letters*, *32*(14), L14704. https://doi.org/10.1029/2005GL023024

Ji, M. X., Huang, J. P., Wang, S. W., Wang, X., Zheng, Z. H., & Ge, J. M. (2008). Winter blocking episodes and impact on climate over East Asia (in Chinese). *Plateau Meteorology*, *27*(2), 415–421.

Kohonen, T. (2001). *Self-organizing maps*. (3rd ed., p. 521). Springer.
Lee, M. H., Lee, S. Y., Song, H. J., & Ho, C. H. (2017). The recent increase in the occurrence of a boreal summer teleconnection and its relationship with temperature extremes. *Journal of Climate*, *30*(18), 7493–7504. https://doi.org/10.1175/JCLI-D-16-0094.1
Lee, S., & Feldstein, S. B. (2013). Detecting ozone- and greenhouse gas-driven wind trends with observational data. *Science*, *339*(6119), 563–567. https://doi.org/10.1126/science.1225154
Leung, Y. T., & Zhou, W. (2015). Variation of circulation and East Asian climate associated with anomalous strength and displacement of the East Asian trough. *Climate Dynamics*, *45*, 2713–2732. https://doi.org/10.1007/s00382-015-2504-6
Liang, S. J., Ding, Y. H., Zhao, N., & Sun, Y. (2014). Analysis of the interdecadal changes of the wintertime surface air temperature over mainland China and regional atmospheric circulation characteristics during 1960–2013 (in Chinese). *Chinese of Journal Atmospheric Science*, *38*(5), 974–992. https://doi.org/10.3878/j.issn.1006-9895.1401.13234
Liang, S. J., Zhao, N., & Ding, Y. H. (2019). Dominant trajectories and influenced regions of the near-surface cold air in the Arctic during positive and negative AO/NAM events (in Chinese). *Chinese Journal of Geophysics*, *62*(1), 19–31. https://doi.org/10.6038/cjg2019M0003
Liu, J., Curry, J. A., Wang, H., Song, M., & Horton, R. M. (2012). Impact of declining Arctic sea ice on winter snowfall. *Proceeding of the National Academy of Sciences of the Unites States of America*, *109*(11), 4074–4079. https://doi.org/10.1073/pnas.1114910109
Liu, Q., Chen, G., Wang, L., Kanno, Y., & Iwasaki, T. (2021). Southward cold airmass flux associated with the East Asian winter monsoon: Diversity and impacts. *Journal of Climate*, 1–37. https://doi.org/10.1175/JCLI-D-20-0319.1
Liu, Q. Y., Liu, Q., & Chen, G. X. (2020). Isentropic analysis of regional cold events over northern China. *Advances in Atmospheric Sciences*, *37*, 718–734. https://doi.org/10.1007/s00376-020-9226-3
Liu, X. D., Yin, Z. Y., Shao, X. M., & Qin, N. S. (2006). Temporal trends and variability of daily maximum and minimum, extreme temperature events, and growing season length over the eastern and central Tibetan Plateau during 1961-2003. *Journal of Geophysical Research*, *111*(D19), D19109. https://doi.org/10.1029/2005jd006915
Luo, D., Xiao, Y., Yao, Y., Dai, A., Simmonds, I., & Franzke, C. L. E. (2016). Impact of Ural blocking on winter warm Arctic-cold Eurasian anomalies. Part I: Blocking-induced amplification. *Journal of Climate*, *29*(11), 3925–3947. https://doi.org/10.1175/JCLI-D-15-0611.1
Ma, S., & Zhu, C. (2019). Extreme cold wave over East Asia in January 2016: A possible response to the larger internal atmospheric variability induced by Arctic warming. *Journal of Climate*, *32*(4), 1203–1216. https://doi.org/10.1175/JCLI-D-18-0234.1
Morgan, C. M., & Nielsen-Gammon, J. W. (1998). Using tropopause maps to diagnose midlatitude weather systems. *Monthly Weather Review*, *126*(10), 2555–2579. https://doi.org/10.1175/1520-0493(1998)126<2555:UTMTDM>2.0.CO;2
Park, T. W., Ho, C. H., & Yang, S. (2011). Relationship between the Arctic Oscillation and cold surges over East Asia. *Journal of Climate*, *24*(1), 68–83. https://doi.org/10.1175/2010JCLI3529.1
Park, T. W., Ho, C. H., Yang, S., & Jeong, J. H. (2010). Influences of Arctic Oscillation and Madden-Julian Oscillation on cold surges and heavy snowfalls over Korea: A case study for the winter of 2009-2010. *Journal of Geophysical Research*, *115*, D23122. https://doi.org/10.1029/2010JD014794
Peng, J., & Bueh, C. (2011). The definition and classification of extensive and persistent extreme cold events in China. *Atmospheric and Oceanic Science Letters*, *4*(5), 281–286. https://doi.org/10.1080/16742834.2011.11446943
Qian, C., Wang, J., Dong, S. Y., Yin, H., Burke, C., Ciavarella, A., et al. (2018). Human influence on the record-breaking cold event in January of 2016 in eastern China. *Bulletin of the American Meteorological Society*, *99*(1), S118–S122. https://doi.org/10.1175/BAMS-D-17-0095.1
Qian, C., Zhang, X., & Li, Z. (2019). Linear trends in temperature extremes in China, with an emphasis on non-Gaussian and serially dependent characteristics. *Climate Dynamics*, *53*, 533–550. https://doi.org/10.1007/s00382-018-4600-x
Qian, W. (2012). *Principles of medium to extended range weather forecasts* (p. 409). Science Press.
Robinson, D. P., & Black, R. X. (2005). The statistics and structure of subseasonal midlatitude variability in NASA GSFC GCMs. *Journal of Climate*, *18*, 3294–3316. https://doi.org/10.1175/jcli3450.1
Shapiro, M. A., & Thorpe, A. J. (2004). *THORPEX International Science Plan* (Vol. *57*). WMO/TD USA.
Song, L., & Wu, R. (2017). Processes for occurrence of strong cold events over eastern China. *Journal of Climate*, *30*(22), 9247–9266. https://doi.org/10.1175/JCLI-D-16-0857.1
Tajie, S. L., Shi, N., Wang, Y. C., & Zhang, D. D. (2020). Interdecadal variation of China's winter extreme cold temperature index (in Chinese). *Chinese Journal of Atmospheric Sciences*, *44*(5), 1125–1140. https://doi.org/10.3878/j.issn.1006-9895.2003.19242
Takaya, K., & Nakaruma, H. (2001). A formulation of a phase-independent wave-activity flux for stationary and migratory quasigeostrophic eddies on a zonally varying basic flow. *Journal of the Atmospheric Sciences*, *58*(6), 608–627. https://doi.org/10.1175/1520-0469(2001)058<0608:AFOAPI>2.0.CO;2
Takaya, K., & Nakaruma, H. (2005). Mechanisms of intraseasonal amplification of the cold Siberian high. *Journal of the Atmospheric Sciences*, *62*(12), 4423–4440. https://doi.org/10.1175/JAS3629.1
Tao, S. Y. (1959). Studies of cold waves over East Asia in China in recent 10 years (in Chinese). *Acta Meteorlogica Sinica*, *30*(3), 226–230.
Thompson, D. W. J., & Wallace, J. M. (1998). The Arctic Oscillation signature in the wintertime geopotential height and temperature fields. *Geophysical Research Letters*, *25*(9), 1297–1300. https://doi.org/10.1029/98GL00950
Wang, L., & Chen, W. (2014). A CMIP5 multimodel projection of future temperature, precipitation, and climatological drought in China. *International Journal of Climatology*, *34*(6), 2059–2078. https://doi.org/10.1002/joc.3822
Wang, L., Chen, W., Huang, G., & Zeng, G. (2017). Changes of the Transitional Climate Zone in East Asia: Past and Future. *Climate Dynamics*, *49*(4), 1463–1477. https://doi.org/10.1007/s00382-016-3400-4
Wang, L., Chen, W., Zhou, W., & Huang, R. (2009). Interannual variations of East Asian trough axis at 500 hPa and its association with the East Asian winter monsoon pathway. *Journal of Climate*, *22*(3), 600–614. https://doi.org/10.1175/2008JCLI2295.1
Wang, X. J., Shen, B. Z., Gong, Z. Q., & Feng, G. L. (2013). The classification of winter regional extreme low temperature events in China and their corresponding relationship to climatic indices extreme anomaly (in Chinese). *Acta Physica Sinica*, *62*(22), 229201. https://doi.org/10.7498/aps.62.229201
Wang, Z. Y., & Ding, Y. H. (2006). Climate change of the cold wave frequency of China in the last 53 years and the possible reasons (in Chinese). *Chinese Journal of Atmospheric Sciences*, *30*(6), 1068–1076.
Ward, J. H. (1963). Hierarchical grouping to optimize an objective function. *Journal of the American Statistical Association*, *58*(301), 236–244. https://doi.org/10.1080/01621459.1963.10500845
Wilks, D. S. (2006). Statistical methods in the atmospheric sciences. *International Geophysics* (2nd ed.). Academic Press.
Wu, B. Y., Yang, K., & Francis, J. A. (2017). A cold event in Asia during January-February 2012 and its possible association with Arctic sea ice loss. *Journal of Climate*, *30*(19), 7971–7990. https://doi.org/10.1175/JCLI-D-16-0115.1
Wu, J. H., & Ren, R. C. (2021). Stratosphere-troposphere interactions during nationwide extensive and persistent extreme cold events in boreal winter (in Chinese). *Chinese Journal of Atmospheric Sciences*, *45*(3), 558–572.

Xie, R. Q., Liu, Y. D., Zhu, J. S., & Meng, T. (2019). Analysis of isentropic potential vorticity for an extreme cold wave event (in Chinese). *Meteorological Science and Technology*, *47*(2), 312–321. https://doi.org/10.19517/j.1671-6345.20170534

Xie, Z., Black, R. X., & Deng, Y. (2017a). The structure and large-scale organization of extreme cold waves over the conterminous Unites States. *Climate Dynamics*, *49*, 4075–4088. https://doi.org/10.1007/s00382-017-3564-6

Xie, Z., Black, R. X., & Deng, Y. (2017b). Daily-scale planetary wave patterns and the modulation of cold season weather in the northern extratropics. *Journal of Geophysical Research*, *122*(16), 8383–8398. https://doi.org/10.1002/2017JD026768

Xie, Z., Black, R. X., & Deng, Y. (2019). Planetary and synoptic-scale dynamic control of extreme cold wave patterns over the United States. *Climate Dynamics*, *53*, 1477–1495. https://doi.org/10.1007/s00382-019-04683-7

Xie, Z., & Bueh, C. (2017). Cold vortex events over Northeast China associated with the Yakutsk-Okhotsk blocking. *International Journal of Climatology*, *37*(1), 381–398. https://doi.org/10.1002/joc.4711

Yasutomi, N., Hamada, A., & Yatagai, A. (2011). Development of a long-term daily gridded temperature dataset and its application to rain/snow discrimination of daily precipitation. *Global Environmental Research*, *15*(2), 165–172.

Ye, D. Z., Tao, S. Y., Zhu, B. Z., Yang, J. C., & Chen, L. X. (1962). *Research on the Northern Hemisphere winter blocking situation (in Chinese)* (pp. 1–2). Science Press.

Yu, B., & Zhang, X. (2015). A physical analysis of the severe 2013/2014 cold winter in North America. *Journal of Geophysical Research*, *120*(19), 10149–10165. https://doi.org/10.1002/2015JD023116

Yuan, C., & Li, W. (2019). Variations in the frequency of winter extreme cold days in northern China and possible causalities. *Journal of Climate*, *32*(23), 8127–8141. https://doi.org/10.1175/JCLI-D-18-0771.1

Zhang, X. B., Hegerl, G., Zwiers, F. W., & Kenyon, J. (2005). Avoiding inhomogeneity in percentile-based indices of temperature extremes. *Journal of Climate*, *18*(11), 1641–1651. https://doi.org/10.1175/JCLI3366.1

Zhang, Z., & Qian, W. (2011). Identifying regional prolonged low temperature events in China. *Advances in Atmospheric Sciences*, *28*, 338–351. https://doi.org/10.1007/s00376-010-0048-6

Zhou, W., Chan, J. C. L., Chen, W., Ling, J., Pinto, J. G., & Shao, Y. (2009). Synoptic-scale controls of persistent low temperature and icy weather over Southern China in January 2008. *Monthly Weather Review*, *137*(11), 3978–3991. https://doi.org/10.1175/2009MWR2952.1

Zhou, Y. Q., & Ren, G. Y. (2010). Variation characteristics of extreme temperature indices in mainland China during 1956-2008 (in Chinese). *Climatic and Environmental Research*, *15*(4), 405–417.